MagnetoHemoDynamics in Aorta and Electrocardiograms

Vincent Martin, Agnès Drochon, Odette Fokapu, Jean-Frédéric Gerbeau

To cite this version:

Vincent Martin, Agnès Drochon, Odette Fokapu, Jean-Frédéric Gerbeau. MagnetoHemoDynamics in Aorta and Electrocardiograms. [Research Report] RR-7747, 2011, pp.38. inria-00628032v1

HAL Id: inria-00628032
https://inria.hal.science/inria-00628032v1
Submitted on 30 Sep 2011 (v1), last revised 23 May 2012 (v2)

HAL is a multi-disciplinary open access archive for the deposit and dissemination of scientific research documents, whether they are published or not. The documents may come from teaching and research institutions in France or abroad, or from public or private research centers.

L'archive ouverte pluridisciplinaire **HAL**, est destinée au dépôt et à la diffusion de documents scientifiques de niveau recherche, publiés ou non, émanant des établissements d'enseignement et de recherche français ou étrangers, des laboratoires publics ou privés.

INSTITUT NATIONAL DE RECHERCHE EN INFORMATIQUE ET EN AUTOMATIQUE

MagnetoHemoDynamics in Aorta and Electrocardiograms

Vincent Martin — Agnès Drochon — Odette Fokapu — Jean-Frédéric Gerbeau

N° 7747

Septembre 2011

Observation, Modeling, and Control for Life Sciences

Rapport
de recherche

ISSN 0249-6399 ISRN INRIA/RR--7747--FR+ENG

INSTITUT NATIONAL
DE RECHERCHE
EN INFORMATIQUE
ET EN AUTOMATIQUE

INRIA

centre de recherche
PARIS - ROCQUENCOURT

MagnetoHemoDynamics in Aorta and Electrocardiograms

Vincent Martin[*][†], Agnès Drochon[‡] , Odette Fokapu[§] [‡],
Jean-Frédéric Gerbeau[†]

Theme : Observation, Modeling, and Control for Life Sciences
Équipe-Projet Reo

Rapport de recherche n° 7747 — Septembre 2011 — 38 pages

Abstract: In presence of a high magnetic field, the blood flow in the aorta induces an electric potential which is responsible for an increase of the T-wave in the electrocardiogram (ECG). This phenomenon may perturb ECG-gated imaging. The aim of this study is to reproduce this experimental observation through computer simulations on a realistic anatomy. The numerical model consists of three compartments: magnetohydrodynamics (MHD) in the aorta, bidomain equations in the heart and electrical diffusion in the rest of the body. These models are strongly coupled together and solved with finite elements. Numerical tests show that this model is actually able to reproduce the expected phenomenon on the ECG.

Key-words: Blood flow, electrophysiology, Magnetohydrodynamics (MHD), MRI, finite elements.

---

[*] University of Technology of Compiègne (UTC), LMAC, GI, Royallieu, BP 20529, 60205 Compiègne, France, Vincent.Martin@utc.fr

[†] INRIA Paris-Rocquencourt, BP 105, 78153 Le Chesnay, France. Jean-Frederic.Gerbeau@inria.fr

[‡] University of Technology of Compiègne (UTC), UMR6600, GB, Royallieu, BP 20529, 60205 Compiègne, France, Agnes.Drochon@utc.fr

[§] Université de Picardie Jules Vernes, Odette.Fokapu@utc.fr

MagnetoHémoDynamique dans l'Aorte et Electrocardiogrammes

Résumé : En présence d'un champ magnétique intense, l'écoulement du sang dans l'aorte induit un potentiel électrique qui est la cause d'une augmentation de l'onde T d'un électrocardiogramme (ECG). Ce phénomène peut perturber l'imagerie médicale synchronisée par ECG.

Le but de cette étude est de reproduire cette observation expérimentale par le biais de simulations numériques sur une anatomie réaliste. Le modèle informatique est constitué de trois compartiments : la magnetohydrodynamique (MHD) dans l'aorte, les équations bidomaine dans le cœur et les équations de l'électrostatique dans le reste du corps. Ces modèles sont fortement couplés ensemble et résolus par la méthode des éléments finis. Les tests numériques montrent que ce modèle est bien capable de reproduire le comportement attendu sur l'ECG.

Mots-clés : Écoulement sanguin, électrophysiologie, magnétohydrodynamique (MHD), MRI, éléments finis.

1 Introduction

In order to improve the quality of the images provided by Magnetic Resonance Imaging (MRI), the magnetic field used in MRI is getting larger and larger: from $3T$ nowadays (for human), it might increase up to $10T$ in the future. We are interested in the effect of this high static magnetic field and, more specifically, in the perturbations induced on the electrocardiogram (ECG). Indeed, the interaction between the blood flow and the magnetic field results in an induced electric field in the arteries. This magnetohydrodynamic (MHD) effect mainly occurs in the aortic arch, because in this location the blood velocity is large and almost orthogonal to the magnetic field (oriented along the main body axis in a MRI machine). The induced voltage may alter the electric potential measured during ECG. In particular, the induced electric field is known to increase the T-wave, which in turn may perturb the ECG-gated image acquisition. Different ways of circumventing this gating issue have been proposed, for instance using VectoCardioGrams (VCG) [6], or acoustic cardiac signal [9], ECG signal processing [32]. However, a better understanding and prediction of the MHD effect would have many potential benefits. First, it may help improve the quality of the ECG, which is not only used for gating but also for clinical purpose, in particular for interventional or exercise stress MRI. Second, the evaluation of the electrical current induced by the magnetic field has an interest *per se*. Third, the MHD artifact might be used to infer some properties of the tissues. This paper is devoted to the modeling and the numerical simulation of this phenomenon and can be viewed as a first step towards these directions.

The interaction of the aortic blood flow and a magnetic field has already been investigated in the literature. An overview of the *in vitro* experiments, *in vivo* studies as well as as MHD calculations in blood flows can be found in [1]. Gaffey *et al.* [10] and Tenforde *et al.* [31] observed animal ECG alterations, manifested mainly as T-wave elevations. Later, the same group provided some simulations of the voltage and current distributions, and resultant reduction in blood flow, by means of a two-dimensional finite element analysis in two sections of the ascending and descending aorta with a conductive wall [18]. They studied the case of a steady state flow with an external magnetic field transverse to the ascending and descending aorta.

More recently, the group of Sahakian *et al.* published a series of papers where the magnetohydrodynamic effect during cardiac MRI was investigated both experimentally [23] and with computer simulations, using Comsol Multiphysics software [25, 24]. A study of MHD was also done in [17]. Another group addressed the problem of ECG simulations in the presence of the magnetic field [15] using the closed-form solution of Gold [13], which corresponds to a steady, fully developed flow of a conducting fluid in a straight cylinder subjected to a transverse magnetic field. In this approach, the aortic arch was divided into slices. In each slice, the Gold solution was used, with a different angle for the magnetic field. The MHD signal was computed from these slices of aorta via a transfer function and then directly added to the ECG waveform that was taken from the ECGSIM software [16].

In the present study, state-of-art mathematical models are considered in each physical compartment of the problem on a realistic anatomy: bidomain equations for the cardiac electrophysiology; inductionless MHD equations for the aortic blood flow; electrostatic equations in the torso, which includes bones and lungs. Contrary to what is usually done in the literature, these three compartments are strongly coupled. This allows in particular to evaluate the possible interaction between the electric potential induced in the aorta and the extracellular potential in the myocardium.

Our numerical simulations show that this model, which produces realistic 12-lead ECG without magnetic field, actually exhibits perturbations of the T-wave in presence of a magnetic field. Due to the complexity of the model and of the multiphysics coupling algorithm, a special effort was dedicated to the verification of the computer implementation. Careful comparisons with the literature or with closed-form solutions will be shown in simplified configurations before addressing the full problem.

The rest of the article is organized as follows: Section 2 is devoted to the mathematical model. In Section 3, the numerical methods are briefly presented, focusing mainly on the MHD part. Section 4 contains the numerical results: three test cases are considered in Section 4.1 for verification purposes, while the main results including the standard ECGs with the MHD effects are shown and discussed in Section 4.2. Section 5 is devoted to the concluding remarks.

The numerical value of the physical parameters are gathered in annexes.

2 Models

Let Ω be a domain representing the whole body (Figure 1) partitioned into three subdomains, the aorta Ω_{A}, the heart Ω_{H} and the complement Ω_{T}, hereafter sometimes called "torso" for the sake of brevity:

$$\overline{\Omega} = \overline{\Omega_{\mathrm{A}}} \cup \overline{\Omega_{\mathrm{H}}} \cup \overline{\Omega_{\mathrm{T}}},$$

where the closure of an open domain ω is denoted by $\overline{\omega}$. The boundary of ω is denoted by $\partial\omega$. The boundary of the aorta $\partial\Omega_{\mathrm{A}}$ is assumed to be entirely included in the torso and divided into an inlet, four outlets and a wall:

$$\partial\Omega_{\mathrm{A}} = \Gamma_{\mathrm{inlet}} \cup \Gamma_{\mathrm{wall}} \cup \Gamma_{\mathrm{outlets}} \subset \overline{\Omega_{\mathrm{T}}}.$$

The inlet Γ_{inlet} is a planar cut in the ascending aorta. The first three outlets $\Gamma_{\mathrm{outlet}_i}$, $i = 1, 2, 3$, are respectively a section of the brachiocephalic artery, the left common carotid artery, and the left subclavian artery. The last outlet $\Gamma_{\mathrm{outlet}_4}$ is a section of the abdominal aorta (Figure 14). The heart boundary is included in the torso domain

$$\partial\Omega_{\mathrm{H}} \subset \overline{\Omega_{\mathrm{T}}},$$

thus the boundary of the torso is partitioned as follows

$$\partial\Omega_{\mathrm{T}} = \partial\Omega_{\mathrm{A}} \cup \partial\Omega_{\mathrm{H}} \cup \Gamma_{\mathrm{ext}},$$

where Γ_{ext} is the body surface. Throughout the article, $\boldsymbol{n}$ will denote a normal unit vector on given surfaces.

Let us briefly remind the main stages of the electrical activity of the myocardium Ω_{H}. During the systole, an electric signal propagates rapidly in the heart (depolarization). This generates an electric potential in Ω_{T} whose recording on a few points of the body surface Γ_{ext} gives the ECG. The first event seen in the ECG, called the P-wave, corresponds to the depolarization of the atria.

This part is not modeled in the present study. Next, the ventricles are depolarized, which corresponds to the QRS-complex in the ECG. The R-wave, which is the largest positive deflection in the first lead, is used for MRI gating. This depolarization triggers the mechanical contraction of the myocardium, which ejects the blood from the left ventricle into the aorta Ω_{A}. Next, the ventricles return to their rest state (repolarization), which gives the last deflection of the ECG, called T-wave. The peak flow in the aortic arch is reached during this phase (Figure 1). The current induced by MHD effect is therefore maximal at this moment.

The rest of this section is devoted to a presentation of the models solved in the aorta Ω_{A}, the heart Ω_{H} and the torso Ω_{T}.

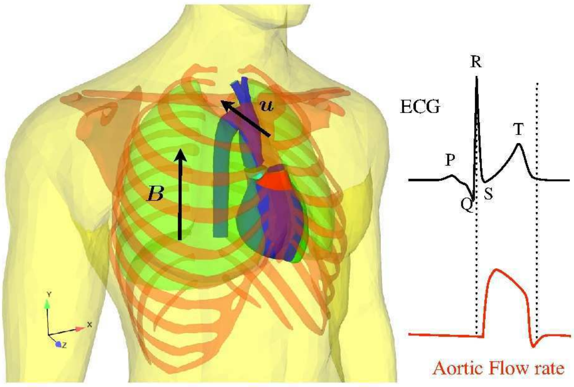

Figure 1: Left: view the three subdomains (aorta, heart and rest of the body, including some bones and the lungs), schematic of the magnetic field $\boldsymbol{B}$ and velocity field $\boldsymbol{u}$ in the aortic arch. Right: First lead of the ECG and aortic flow rate.

2.1 MHD in the aorta

In presence of an electric field $\boldsymbol{E}$ and a magnetic field $\widetilde{\boldsymbol{B}}$, Ohm's law in the blood reads

$$\boldsymbol{j} = \boldsymbol{\sigma}_{\mathrm{bl}}(\boldsymbol{E} + \boldsymbol{u} \times \widetilde{\boldsymbol{B}})$$

where $\boldsymbol{j}$ denotes the current density, $\boldsymbol{\sigma}_{\mathrm{bl}}$ the electrical conductivity of the blood and $\boldsymbol{u}$ the blood velocity. Neglecting the displacement current $\epsilon_0 \partial_t \boldsymbol{E}$ (with the permittivity ϵ_0), the Maxwell-Ampère equation gives another expression of the current density:

$$\boldsymbol{j} = \mathbf{curl}\, \frac{\widetilde{\boldsymbol{B}}}{\mu}, \tag{1}$$

where μ is the magnetic permeability, supposed to be that of the vacuum ($\mu = \mu_0 = 4\pi 10^{-7} H\, m^{-1}$). Inserting these two expressions in the Maxwell-Faraday equation

$$\partial_t \widetilde{\boldsymbol{B}} + \mathbf{curl}\, \boldsymbol{E} = 0, \tag{2}$$

we obtain the usual MHD equations:

$$\begin{cases} \rho\left(\dfrac{\partial \boldsymbol{u}}{\partial t}+\boldsymbol{u}\cdot\boldsymbol{\nabla}\boldsymbol{u}\right)-\eta\Delta\,\boldsymbol{u}+\boldsymbol{\nabla}p=\dfrac{1}{\mu_0}\mathbf{curl}\,\widetilde{\boldsymbol{B}}\times\widetilde{\boldsymbol{B}}, \\ \operatorname{div}\boldsymbol{u}=0, \\ \dfrac{\partial\widetilde{\boldsymbol{B}}}{\partial t}+\mathbf{curl}\left(\dfrac{1}{\mu_0\boldsymbol{\sigma}_{\mathrm{bl}}}\mathbf{curl}\,\widetilde{\boldsymbol{B}}\right)=\mathbf{curl}\,(\boldsymbol{u}\times\widetilde{\boldsymbol{B}}), \end{cases} \tag{3}$$

where p denotes the pressure of the blood, η its viscosity, ρ its density. The right-hand side of the Navier-Stokes equation corresponds to the Lorentz force $\boldsymbol{j}\times\boldsymbol{B}$, with $\boldsymbol{j}$ given by (1).

System (3) is typically used for fluid with a high electrical conductivity, like liquid metals, but is not very convenient for blood flows. Indeed, the magnetic Reynolds number Rm, which is the dimensionless ratio of magnetic advection to magnetic diffusion, is extremely small in that case (Tables 1 and 2). As a consequence, the magnetic field is almost unaffected by the blood flow. In this regime, it is adequate to assume that $\widetilde{\boldsymbol{B}}$ is equal to $\boldsymbol{B}$, the external imposed magnetic field, neglecting the MHD effect on $\boldsymbol{B}$. In an MRI device, $\boldsymbol{B}$ is mainly homogeneous and constant in time. Thus, if $\widetilde{\boldsymbol{B}}\approx\boldsymbol{B}$, the Maxwell-Faraday equation (2) gives $\mathbf{curl}\,\boldsymbol{E}=0$, and there exists an electric potential ϕ_{A} such that

$$\boldsymbol{E}=-\boldsymbol{\nabla}\phi_{\mathrm{A}}.$$

With this expression of $\boldsymbol{E}$, and neglecting again the variations of $\widetilde{\boldsymbol{B}}$ caused by the induction, Ohm's law reads

$$\boldsymbol{j}=\boldsymbol{\sigma}_{\mathrm{bl}}(-\boldsymbol{\nabla}\phi_{\mathrm{A}}+\boldsymbol{u}\times\boldsymbol{B}). \tag{4}$$

Using this relation in the Lorentz force, and writing the conservation of the electrical charges $\operatorname{div}\boldsymbol{j}=0$, we obtain a simplified form of MHD equations, sometimes called *inductionless MHD* equations,

$$\begin{cases} \rho\left(\dfrac{\partial \boldsymbol{u}}{\partial t}+\boldsymbol{u}\cdot\boldsymbol{\nabla}\boldsymbol{u}\right)-\eta\Delta\,\boldsymbol{u}+\boldsymbol{\nabla}p=-\boldsymbol{\sigma}_{\mathrm{bl}}\boldsymbol{\nabla}\phi_{\mathrm{A}}\times\boldsymbol{B}+\boldsymbol{\sigma}_{\mathrm{bl}}\,(\boldsymbol{u}\times\boldsymbol{B})\times\boldsymbol{B}, \\ \operatorname{div}\boldsymbol{u}=0, \\ \operatorname{div}\left(\boldsymbol{\sigma}_{\mathrm{bl}}\boldsymbol{\nabla}\phi_{\mathrm{A}}\right)=\operatorname{div}\left(\boldsymbol{\sigma}_{\mathrm{bl}}\boldsymbol{u}\times\boldsymbol{B}\right), \end{cases} \tag{5}$$

all these equations being set in Ω_{A}.

In the blood flow regime, system (5) is an excellent approximation of (3) for a wide range of $\boldsymbol{B}$, as will been shown by numerical simulations in Section 4.1. Moreover, it is numerically better conditioned, less expensive to solve, and it provides directly the electric potential, which is the quantity of interest for the electrocardiograms.

Fluid boundary conditions. A time dependent plug flow is applied at the inlet of the aorta, a no-slip condition is applied on the wall, and a pressure is applied at the four outlets:

$$\begin{cases} \boldsymbol{u} &= \boldsymbol{u}_{\mathrm{inlet}}, & \text{on } \Gamma_{\mathrm{inlet}}, \\ \boldsymbol{u} &= 0, & \text{on } \Gamma_{\mathrm{wall}}, \\ p &= \overline{p}_i & \text{on } \Gamma_{\mathrm{outlet_i}}, i=1,..,4. \end{cases} \tag{6}$$

	Parameters	Value	Units
ρ	blood density	1000	$kg\ m^{-3}$
η	blood dynamic viscosity	0.005	$Pa\ s$
$\boldsymbol{\sigma}_{\mathrm{bl}}$	blood elec. conductivity	0.5	$S\ m^{-1}$
B_0	magnetic field	1.	$Tesla$
L_0	length scale	0.01	m
T_0	time scale	1	s
U_0	blood velocity	L_0/T_0	$m\ s^{-1}$
		0.01	$m\ s^{-1}$
Φ_0	electric potential	$U_0 B_0 L_0$	V
		10^{-4}	V
σ_0	ref. elec. conductivity	$\boldsymbol{\sigma}_{\mathrm{bl}}$	$S\ m^{-1}$
μ_0	magnetic permeability	$4\pi 10^{-7}$	$N\ A^{-2}$
P_0	reference pressure	ρU_0^2	Pa
		0.1	Pa

Table 1: Order of magnitude of the blood flow parameters in the international system.

Numbers	Symbol	Definition	Value
Reynolds	Re	$\dfrac{\rho U_0 L_0}{\eta}$	20
Magnetic Rey.	Rm	$\mu_0 \sigma_0 U_0 L_0$	6.10^{-11}
Hartmann	Ha	$B_0 L_0 \sqrt{\dfrac{\sigma_0}{\eta}}$	0.1

Table 2: Typical values of the MHD numbers.

The outlet pressure $\overline{p}_i$ is obtained by coupling a three-element Windkessel model (see for example [8]) to the Navier-Stokes equations. More precisely,

$$\overline{p}_i = \pi_i + R_{p,i} Q_i$$

where Q_i is the volumetric flow rate,

$$Q_i = \int_{\Gamma_{\mathrm{outlet}_\mathrm{i}}} \boldsymbol{u} \cdot \boldsymbol{n} \, dS,$$

and π_i is the solution to the ordinary differential equation

$$C_i \frac{d\pi_i}{dt} + \frac{\pi_i}{R_{d,i}} = Q_i.$$

The parameters $R_{d,i}$, $R_{p,i}$ and C_i represent the distal resistance, the proximal resistance and the capacitance C_i respectively. The coefficients that are used in our simulations are taken from [21] and are reported in Table 12.

We postpone the definition of the boundary conditions for ϕ_{A} to Section 2.4, where the transmission conditions for the three compartments will be presented together.

2.2 Electrophysiology in the heart

We denote by ϕ_{H} and V_{m} the extracellular potential and the transmembrane potential, and by $\boldsymbol{\sigma}_{\mathrm{i}}$ and $\boldsymbol{\sigma}_{\mathrm{e}}$ the intra- and extracellular conductivity tensors.

In the heart Ω_{H}, the electrical activity is governed by the bidomain equations [28, 29]:

$$\begin{cases} A_{\mathrm{m}}\left(C_{\mathrm{m}}\dfrac{\partial V_{\mathrm{m}}}{\partial t}+I_{\mathrm{ion}}(V_{\mathrm{m}},w)\right)-\mathrm{div}(\boldsymbol{\sigma}_{\mathrm{i}}\boldsymbol{\nabla}V_{\mathrm{m}})-\mathrm{div}(\boldsymbol{\sigma}_{\mathrm{i}}\boldsymbol{\nabla}\phi_{\mathrm{H}})=A_{\mathrm{m}}I_{\mathrm{app}}, \\ -\mathrm{div}((\boldsymbol{\sigma}_{\mathrm{i}}+\boldsymbol{\sigma}_{\mathrm{e}})\boldsymbol{\nabla}\phi_{\mathrm{H}})-\mathrm{div}(\boldsymbol{\sigma}_{\mathrm{i}}\boldsymbol{\nabla}V_{\mathrm{m}})=0, \end{cases} \tag{7}$$

where A_{m} is a constant representing the rate of membrane area per volume unit and C_{m} the membrane capacitance per area unit. In (7), the first equation represents the homogenized cell membrane activity and the second equation the conservation of the total electrical current (intra and extracellular). The term $I_{\mathrm{ion}}(V_{\mathrm{m}},w)$ represents the ionic current through the cell membranes, and I_{app} is a given source term. The dynamics of the ionic variable w and the ionic current I_{ion} are governed by the phenomenological two-variable model proposed by Mitchell and Schaeffer in [20]:

$$I_{\mathrm{ion}}(V_{\mathrm{m}},w)=-\frac{w}{\tau_{\mathrm{in}}}\frac{(V_{\mathrm{m}}-V_{\mathrm{min}})^2(V_{\mathrm{max}}-V_{\mathrm{m}})}{V_{\mathrm{max}}-V_{\mathrm{min}}}+\frac{1}{\tau_{\mathrm{out}}}\frac{V_{\mathrm{m}}-V_{\mathrm{min}}}{V_{\mathrm{max}}-V_{\mathrm{min}}}, \tag{8}$$

and

$$g(V_{\mathrm{m}},w)=\begin{cases} \dfrac{w}{\tau_{\mathrm{open}}}-\dfrac{1}{\tau_{\mathrm{open}}(V_{\mathrm{max}}-V_{\mathrm{min}})^2} & \text{if} \quad V_{\mathrm{m}}<V_{\mathrm{gate}}, \\ \dfrac{w}{\tau_{\mathrm{close}}} & \text{if} \quad V_{\mathrm{m}}>V_{\mathrm{gate}}, \end{cases} \tag{9}$$

where τ_{in}, τ_{out}, τ_{open}, τ_{close}, V_{gate} are given parameters and V_{min}, V_{max} scaling constants (typically -80 and 20 mV, respectively). The ventricles are subdivided into four different regions where the coefficient τ_{close} takes different values. The atria are not considered here, which explains the absence of P-wave in our ECGs. The initial activation starts from the septum. We refer to [3] for more details.

On the boundary of the heart, the intracellular medium is assumed to be isolated,

$$\boldsymbol{\sigma}_{\mathrm{i}}\boldsymbol{\nabla}V_{\mathrm{m}}\cdot\boldsymbol{n}+\boldsymbol{\sigma}_{\mathrm{i}}\boldsymbol{\nabla}\phi_{\mathrm{H}}\cdot\boldsymbol{n}=0 \quad \text{on} \quad \partial\Omega_{\mathrm{H}}. \tag{10}$$

Other boundary conditions are necessary to close the system and will be given in Section 2.4.

2.3 Electric diffusion in the body

To obtain the electrocardiograms, the electric potential has to be computed on the surface of the body. For that purpose, we solve the electrostatic equation satisfied by ϕ_{T} in Ω_{T}:

$$\begin{cases} \mathrm{div}(\boldsymbol{\sigma}_{\mathrm{T}}\boldsymbol{\nabla}\phi_{\mathrm{T}}) = 0, & \text{in} \quad \Omega_{\mathrm{T}}, \\ \boldsymbol{\sigma}_{\mathrm{T}}\boldsymbol{\nabla}\phi_{\mathrm{T}}\cdot\boldsymbol{n} = 0, & \text{on} \quad \Gamma_{\mathrm{ext}}, \end{cases} \tag{11}$$

where the conductivity $\boldsymbol{\sigma}_{\mathrm{T}}$ takes different values in the different regions of the torso (see Table 13). The boundary condition on the internal boundaries $\partial\Omega_{\mathrm{H}}$ and $\partial\Omega_{\mathrm{A}}$ are set in Section 2.4.

2.4 Coupling the three models together

To close the system, the continuity of the potential and of the normal current are imposed at the interfaces between the aorta and the torso $\partial\Omega_\mathrm{A}$

$$\begin{cases} \boldsymbol{\sigma}_\mathrm{bl}\boldsymbol{\nabla}\phi_\mathrm{A}\cdot\boldsymbol{n} = \boldsymbol{\sigma}_\mathrm{T}\boldsymbol{\nabla}\phi_\mathrm{T}\cdot\boldsymbol{n}, \\ \phi_\mathrm{A} = \phi_\mathrm{T}, \end{cases} \tag{12}$$

and at the interface between the heart and the torso $\partial\Omega_\mathrm{H}$

$$\begin{cases} \boldsymbol{\sigma}_\mathrm{e}\boldsymbol{\nabla}\phi_\mathrm{H}\cdot\boldsymbol{n} = \boldsymbol{\sigma}_\mathrm{T}\boldsymbol{\nabla}\phi_\mathrm{T}\cdot\boldsymbol{n}, \\ \phi_\mathrm{H} = \phi_\mathrm{T}. \end{cases} \tag{13}$$

Equations (5), (7) and (11), supplemented with the boundary conditions (6) and (10), are strongly coupled together by the transmission conditions (12)-(13). This makes the global model particularly challenging from a scientific computing standpoint.

Remark 2.1 *In the literature, it is sometimes assumed that the extracellular medium is isolated, i.e.* $\boldsymbol{\sigma}_\mathrm{e}\boldsymbol{\nabla}\phi_\mathrm{H}\cdot\boldsymbol{n} = 0$ *on* $\partial\Omega_\mathrm{H}$. *This assumption considerably simplifies the problem since it decouples the resolution in the heart and in the torso. But, as noticed in [3], this simplification has some impacts on the electrocardiograms. In particular, it significantly increases the amplitude of the ECG. Since our goal is to capture the modification of the amplitude of the signal, we wish to avoid as far as possible* a priori *simplifications that might affect the ECGs.*

3 Numerical methods

This section is devoted to a brief presentation of the time schemes and the coupling algorithm.

Let N be a positive integer, $T > 0$ the final time and $\tau = T/N$ the time step. Given adequate initial conditions, the discrete solutions $\boldsymbol{u}_h^n$, p_h^n and $\phi_{\mathrm{A},h}^n$ are computed in the aorta, $V_{\mathrm{m},h}^n$ and $\phi_{\mathrm{H},h}^n$ in the heart and $\phi_{\mathrm{T},h}^n$ in the torso, for $n = 1, \ldots, N$.

3.1 Aorta

The MHD model of the aorta (5) is solved with P1 finite elements (*i.e.* continuous and piecewise linear functions) for the velocity, the pressure and the electric potential. The incompressibility is enforced with a Chorin-Temam fractional step method [14]. The advection is stabilized with a standard streamline diffusion term. The MHD coupling is explicit in time: the fluid is solved with the electric potential of the previous time step; then the electric potential is computed with the updated velocity. This gives the following numerical scheme for one time step: given $\boldsymbol{u}_h^n$, p_h^n and $\phi_{\mathrm{A},h}^n$, compute $(\boldsymbol{u}_h^{n+1}, p_h^{n+1}, \phi_{\mathrm{A},h}^{n+1})$ in Ω_A

such that

$$\begin{cases} \rho\left(\dfrac{\boldsymbol{u}_h^{n+1}-\boldsymbol{u}_h^n}{\tau}+\boldsymbol{u}_h^n\cdot\boldsymbol{\nabla}\boldsymbol{u}_h^{n+1}\right)-\eta\Delta\,\boldsymbol{u}_h^{n+1}-\boldsymbol{\sigma}_{\mathrm{bl}}\left(\boldsymbol{u}_h^{n+1}\times\boldsymbol{B}\right)\times\boldsymbol{B}= \\ \qquad\qquad\qquad\qquad -\boldsymbol{\nabla}p_h^n-\boldsymbol{\sigma}_{\mathrm{bl}}\boldsymbol{\nabla}\phi_{\mathrm{A},h}^n\times\boldsymbol{B}, \\ \Delta\,p_h^{n+1}=\dfrac{\rho}{\tau}\operatorname{div}\boldsymbol{u}_h^{n+1}, \\ \operatorname{div}\left(\boldsymbol{\sigma}_{\mathrm{bl}}\boldsymbol{\nabla}\phi_{\mathrm{A},h}^{n+1}\right)=\operatorname{div}\left(\boldsymbol{\sigma}_{\mathrm{bl}}\boldsymbol{u}_h^{n+1}\times\boldsymbol{B}\right). \end{cases} \tag{14}$$

As the three unknowns are not solved simultaneously, this scheme is quite efficient.

Two other numerical schemes were also considered during the verification procedure. They consist of solving the Navier-Stokes equation in a monolithic $(\boldsymbol{u}_h^{n+1}, p^{n+1})$ formulation, and of coupling the potential either implicitly ($\theta = 1$ in (15)), or explicitly ($\theta = 0$):
given $\boldsymbol{u}_h^n$ (and $\phi_{\mathrm{A},h}^n$ when $\theta = 0$), compute $(\boldsymbol{u}_h^{n+1}, p_h^{n+1}, \phi_{\mathrm{A},h}^{n+1})$ in Ω_{A} such that

$$\begin{cases} \rho\left(\dfrac{\boldsymbol{u}_h^{n+1}-\boldsymbol{u}_h^n}{\tau}+\boldsymbol{u}_h^n\cdot\boldsymbol{\nabla}\boldsymbol{u}_h^{n+1}\right)-\eta\Delta\,\boldsymbol{u}_h^{n+1}-\boldsymbol{\sigma}_{\mathrm{bl}}\left(\boldsymbol{u}_h^{n+1}\times\boldsymbol{B}\right)\times\boldsymbol{B}+\boldsymbol{\nabla}p_h^{n+1}= \\ \qquad\qquad\qquad\qquad\qquad\qquad -\boldsymbol{\sigma}_{\mathrm{bl}}\boldsymbol{\nabla}\phi_{\mathrm{A},h}^{n+\theta}\times\boldsymbol{B}, \\ \operatorname{div}\boldsymbol{u}_h^{n+1}=0, \\ \operatorname{div}\left(\boldsymbol{\sigma}_{\mathrm{bl}}\boldsymbol{\nabla}\phi_{\mathrm{A},h}^{n+1}\right)=\operatorname{div}\left(\boldsymbol{\sigma}_{\mathrm{bl}}\boldsymbol{u}_h^{n+1}\times\boldsymbol{B}\right). \end{cases} \tag{15}$$

A stabilization term is added to deal with the equal order approximation of the pressure and the velocity. This scheme is more expensive than (14) but is expected to have better stability properties, especially in the case $\theta = 1$.

We observed that with the physical parameters of blood flows and with the time step needed for the bidomain equations, algorithm (14) proves to be stable and accurate (see Section 4.1). Since it is much more efficient than (15), it will the one used to solve the full problem.

3.2 Heart and Body

The electrical heart model (7) is also solved with P1 finite element. The system is discretized in time by combining a second order Backward Differentiation Formula (BDF2) implicit scheme with an explicit treatment of the ionic current, as proposed in [3]. In the rest of the body, the Laplace equation (11) is solved with the same finite element.

3.3 Coupling

The interface conditions (12)-(13) strongly couple the discrete counterparts of equations (5), (7) and (11) together. The coupling of the three components of the model is performed using a Dirichlet-Neumann domain decomposition algorithm (see for instance [27]), the interface linear problem being solved by a matrix-free GMRES algorithm. The matrix-vector product of the interface problem is computed as represented in Figure 2: at each time step, the potentials coming from the aorta and the heart are sent to the torso where a Dirichlet problem is solved; then the torso sends back the variational form of the electrical current to the aorta and to the heart where a Neumann problem is solved; these iterations are repeated until convergence before going to the next time step. The "weak" coupling strategy is also reported in Figure 2. It essentially consists of doing only one iteration of the domain decomposition algorithm, starting with the homogeneous Neumann problems in the aorta and in the heart.

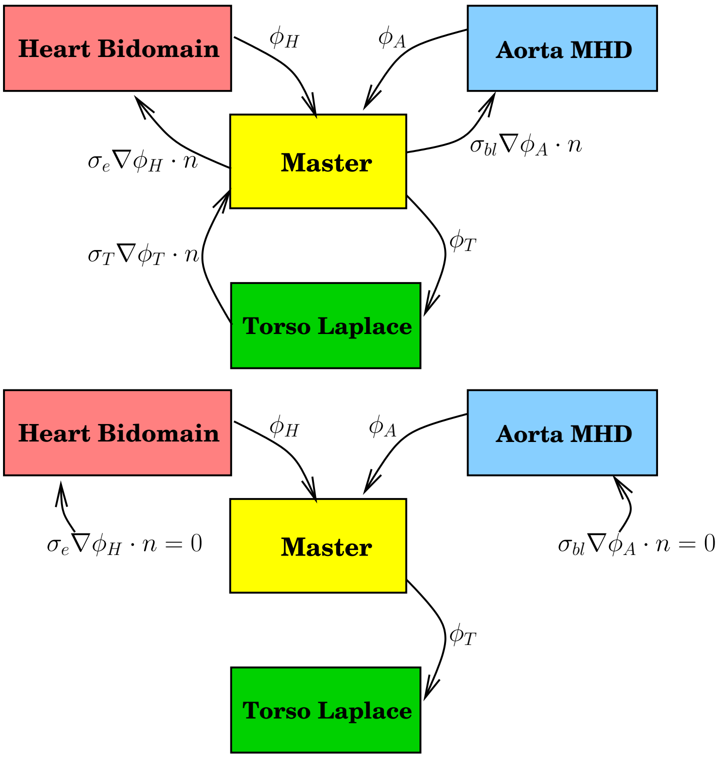

Figure 2: Coupling strategy. Top: Dirichlet-Neumann algorithm. Bottom: "weak" coupling: there is no feedback between the torso on the one hand, and the heart and the aorta on the other hand.

4 Numerical results

4.1 Verification tests

In this section, we consider some tests to verify the correctness of our MHD solver, the validity of the inductionless approximation of the MHD equations in blood flow regime, the coupling strategy with the Poisson equation.

For the sake of simplicity, system (5) is replaced by its stationary linear counterpart (in this section only):

$$\left\{\begin{aligned} -\eta \Delta \boldsymbol{u} + \boldsymbol{\nabla} p &= -\,\sigma \boldsymbol{\nabla} \phi \times \boldsymbol{B} + \sigma\,(\boldsymbol{u} \times \boldsymbol{B}) \times \boldsymbol{B}, \\ \operatorname{div} \boldsymbol{u} &= 0, \\ \operatorname{div}\,(\sigma \boldsymbol{\nabla} \phi) &= \operatorname{div}\,(\sigma \boldsymbol{u} \times \boldsymbol{B})\,, \end{aligned}\right. \tag{16}$$

in a domain Ω.

4.1.1 Comparison with an analytical solution: pseudo-Hartmann 2d flow

We consider problem (16) in the 2D domain $\Omega = [0, L_x = 1] \times [0, L_y]$ (Figure 3, Left). The static magnetic field is oriented along Oz, $\boldsymbol{B} = [0, 0, B_0]^\top$. A no-slip condition $\boldsymbol{u} = 0$ is imposed on $y = 0$ and $y = L_y$, while a pressure gradient G is imposed between the inlet and the outlet.

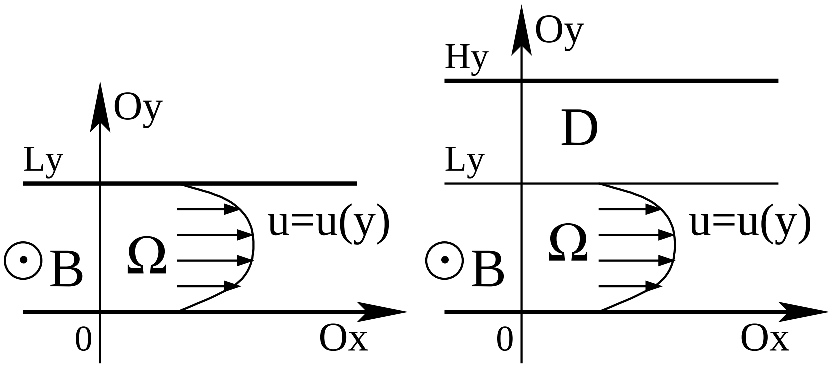

Figure 3: Hartmann 2d validation: description of the configurations. Left: tube Ω alone. Right: tube Ω with a diffusive domain D above.

This configuration is similar to a Hartmann flow [12, 22], however it differs in two ways. Firstly, the standard Hartmann solutions usually refer to the original MHD equations (3), whereas we consider here its inductionless approximation (5). Secondly, the static magnetic field $\boldsymbol{B}$ is not imposed along the usual direction Oy but along Oz. Note that the analytical solution to (5) is less interesting with $\boldsymbol{B}$ along Oy, since the potential and the velocity are then decoupled.

The velocity can be written as $\boldsymbol{u} = [u(y), 0, 0]^\top$, while the pressure is linear in x, $p = -Gx$, and the electric potential only depends on y, $\phi = \phi(y)$. Thus system (16) is reduced to

$$\begin{aligned} -\eta u''(y) + \sigma B_0^2 u(y) - G &= -\sigma B_0 \phi'(y) \\ \phi''(y) &= -B_0 u'(y). \end{aligned} \tag{17}$$

We deduce that $u''' = 0$, implying that

$$u = Cy(L_y - y),$$

with some constant C, and $\phi' = -B_0 u + K$, with another constant K. Inserting the last expression into $(17)_1$, we obtain the relation $K = \dfrac{G - 2C\eta}{\sigma B_0}$, thus

$$\phi = C B_0 \frac{y^3}{3} - C B_0 L_y \frac{y^2}{2} + \frac{G - 2C\eta}{\sigma B_0} y + \phi_0,$$

where ϕ_0 is a constant.

To close the system and determine the constants ϕ_0 and C, the electric boundary conditions have to be specified. Two cases are considered in the next paragraphs.

Imposed potentials Assuming that the boundary conditions $\phi(0) = \phi_0$ and $\phi(L_y) = \phi_0 + \delta\phi$ are imposed, with given constants ϕ_0 and $\delta\phi$, we obtain

$$C = \frac{6}{\eta} \frac{G - \sigma B_0 \, \delta\phi / L_y}{12 + (\sigma/\eta) B_0^2 L_y^2}.$$

The comparison between this analytical solution and the numerical result is presented in Figure 4. The stationary numerical and analytical solutions can hardly be distinguished.

Some transient simulations were computed using the three numerical schemes (14), (15) with $\theta = 0$ and $\theta = 1$. The boundary conditions are identical and remain constant in time. The solutions start from 0 and are iterated in time until reaching a stationary state. As expected the transient numerical solutions converge in time towards the stationary solution.

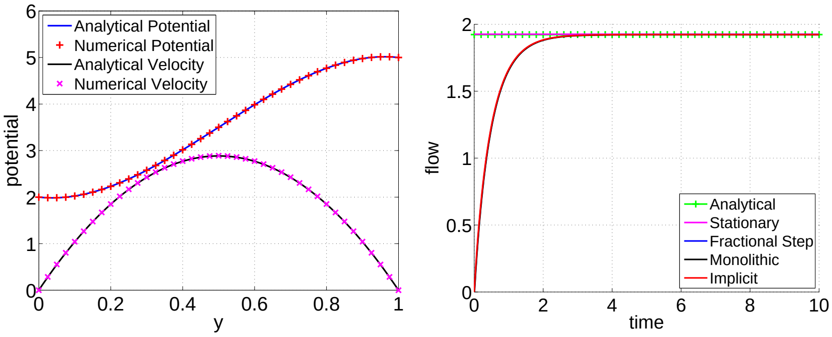

Figure 4: Hartmann 2d validation. Dirichlet boundary conditions. Left: velocity (parabola) and potential as a function of y; comparison between analytical (solid line) and numerical (crosses) solutions. Right: inlet flux as a function of time, comparison between stationary analytical solution and numerical solutions. The curves corresponding to the different numerical methods (fractional step: (14), monolithic: (15) with $\theta = 0$, implicit: (15) with $\theta = 1$) are almost superimposed. Arbitrary values: $B_0 = -2$, $\sigma = 0.5$, $\eta = 0.05$, $\phi_0 = 2$, $\delta\phi = 3, G = 2$, $L_y = 1$. Time step $\tau = 10^{-2}$.

Coupling with a Poisson equation In order to verify the multi-domain coupling algorithm, we now supplement the domain Ω with the domain $D = [0, L_x] \times [L_y, H_y]$, $(H_y > L_y)$ where no fluid flows, but where the potential satisfies a Poisson equation (Figure 3, Right). This configuration roughly mimics the aorta and the torso. The coupling between the two domains is done as explained in Section 3.3.

In D, the potential satisfies

$$-\operatorname{div}(\sigma \boldsymbol{\nabla} \phi) = 0,$$

with the boundary conditions $\phi(0) = \phi_0$ and $\phi(H_y) = \phi_0 + \delta\phi$, where ϕ_0 and $\delta\phi$ are two given constants. We deduce that $\phi = \alpha(y - H_y) + \phi_0 + \delta\phi$. To close the system, we write the transmission conditions (12) in $y = L_y$:

$$\phi'(L_y) = \alpha = -B_0 u(L_y) + K = K,$$

and

$$\begin{aligned}\phi(L_y) - \phi_0 &= \alpha(L_y - H_y) + \delta\phi \\ &= -CB_0 L_y^3/6 + KL_y.\end{aligned}$$

We obtain

$$C = \frac{6}{\eta}\,\frac{G - \sigma B_0\,\delta\phi/H_y}{12 + (\sigma/\eta)B_0^2 L_y^3/H_y},$$

and

$$\phi = \begin{cases} CB_0\dfrac{y^3}{3} - CB_0 L_y\dfrac{y^2}{2} + \dfrac{G - 2C\eta}{\sigma B_0}y + \phi_0, & y \le L_y, \\ \dfrac{G - 2C\eta}{\sigma B_0}(y - H_y) + \phi_0 + \delta\phi, & y \ge L_y. \end{cases}$$

The analytical and the numerical solutions are in good agreement (Figure 5).

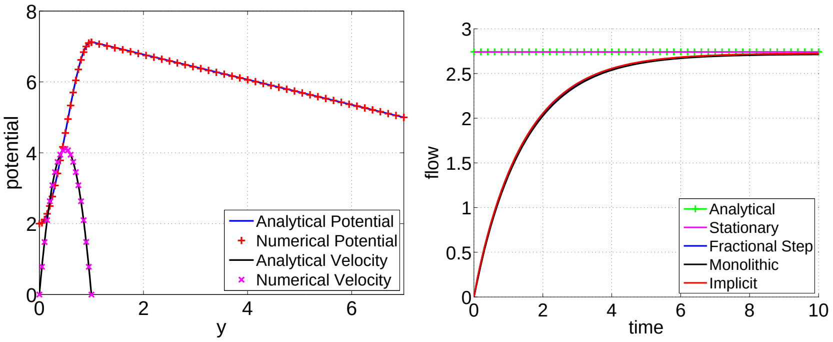

Figure 5: Hartmann 2d validation. MHD coupled to a diffusive domain. Left: velocity (parabola) and potential as a function of y; comparison between analytical (solid line) and numerical (crosses) solutions. The velocity is only represented in the fluid domain. Right: inlet flux as a function of time, comparison between the stationary analytical solution and the numerical solutions. The curves corresponding to the different numerical methods (fractional step: (14), monolithic: (15) with $\theta = 0$, implicit: (15) with $\theta = 1$) are almost superimposed. $B_0 = -2,\ \sigma = 0.5,\ \eta = 0.05,\ \phi_0 = 2,\ \delta\phi = 3, G = 2,\ L_y = 1, H_y = 7$. Time step $\tau = 10^{-2}$.

4.1.2 Comparison with an analytical solution: non-conducting straight tube (Gold)

Gold [13] provides the solution of the steady flow of an incompressible, viscous, electrically conducting fluid through a circular pipe in the presence of an applied transverse uniform magnetic field. A no-slip condition on the velocity is assumed at the non-conducting wall. The analytical solution (mean flow, velocity, electric potential along a diameter) is computed as a series of modified Bessel functions of the first kind [1]. The numerical values of the analytical solutions were obtained using truncated series.

We consider a physical configuration close to the blood flows. The domain Ω is a straight cylinder of radius $R = 1\ cm$ and oriented along the Oz axis. The viscosity is $\eta = 0.05$ Poise and the conductivity is $\sigma = 5.10^{-3}\, S\, cm^{-1}$. A pressure gradient $G = -\dfrac{dp}{dz} = 24\, g\, cm^{-2}\, s^{-2}$ is imposed between the inlet and the outlet. A static magnetic field of intensity $\boldsymbol{B} = 0, 10, 100\ T$ is imposed along the Ox axis. The wall is insulating and, by symmetry, the potential does not depend on z. The boundary conditions are thus

$$\begin{cases} \boldsymbol{u} = 0 & \text{on } \Gamma_{\text{wall}}, \\ p(z = L) = LG & \text{on } \Gamma_L, \\ p(z = 0) = 0 & \text{on } \Gamma_0, \\ \nabla\phi \cdot \boldsymbol{n} = 0 & \text{on } \partial\Omega. \end{cases} \tag{18}$$

Four different levels of refinement were considered, from the coarsest mesh, denoted M_1 to the finest one denoted M_4, see Table 3.

Mesh	# vertices	# tetrahedra
M_1	16 000	88 000
M_2	66 000	380 000
M_3	140 000	800 000
M_4	265 000	1 500 000

Table 3: Meshes for the Gold test-case.

The Table 4 summarizes the results: the flux, the maximum axial velocity, the transverse difference of electric potential and the maximum electrical current modulus are given as a function of $\boldsymbol{B}$, or the Hartmann number defined here as $Ha = \boldsymbol{B}R\sqrt{\sigma/\eta} = 0.1\boldsymbol{B}$. Note that according to these computations, the flow reduction between $\boldsymbol{B} = 0T$ and $\boldsymbol{B} = 10T$ is approximately 2%. The impact of the magnetic field on the flow is therefore very small. A plot of the norm of the velocity, of the potential and of the electrical current modulus is shown in Figures 6, 7 and 8. For $\boldsymbol{B} = 10T$ and $\boldsymbol{B} = 100T$, the numerical results are in excellent agreement with the analytical solution.

These results confirm the validity of the inductionless approximation for MHD in blood flows with $\boldsymbol{B}$ ranging from 0 to $100T$. Abi-Abadallah *et al.* [1] also reached the same conclusion.

Some transient simulations starting from 0 are performed on the mesh M_2 using the three schemes (14) and (15) for $\theta = 0$ and 1. In Figure 9, the maximum velocity and the potential are represented as a function of time for $\boldsymbol{B} = 0$, 10, and $100\,T$. The stationary analytical solutions are also reported. The transient values actually tend to the correct numerical stationary state, as expected. Moreover the three numerical schemes have almost the same behavior.

	B (T)	Ha	Flux $(cm^3\ s^{-1})$	$V_{\max}$ $(cm\ s^{-1})$	$\Delta\phi$ (mV)	$\lVert\boldsymbol{j}\rVert^{\max}$ $(A\ m^{-2})$
exact	0	0	188.496	120	0	0
M_1	0	0	187.08	119.37	0	0
M_2	0	0	188.02	119.79	0	0
M_3	0	0	188.20	119.92	0	0
M_4	0	0	188.29	119.91	0	0
exact	10	1	184.706	116.400	117.389	2.9546
M_1	10	1	183.30	115.79	117.01	2.973
M_2	10	1	184.24	116.20	117.30	2.970
M_3	10	1	184.41	116.32	117.34	2.968
M_4	10	1	184.50	116.31	117.36	2.965
exact	100	10	90.634	42.882	550.171	16.6321
M_1	100	10	89.02	42.21	542.99	16.45
M_2	100	10	90.06	42.65	547.75	16.61
M_3	100	10	90.27	42.74	548.67	16.64
M_4	100	10	90.39	42.78	549.22	16.65

Table 4: Gold validation: comparison between analytical results and numerical results on various mesh refinements M_i, $i = 1, \dots, 4$.

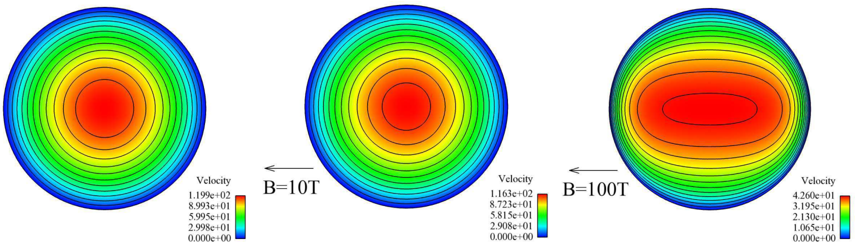

Figure 6: Gold validation. Norm of velocity along a transverse cutplane. Left: $\boldsymbol{B} = 0\,T$, scale $[0, 119.9] cm\ s^{-1}$. Center: $\boldsymbol{B} = 10\,T$, scale $[0, 116.3] cm\ s^{-1}$. Right: $\boldsymbol{B} = 100\,T$, scale $[0, 42.6] cm\ s^{-1}$.

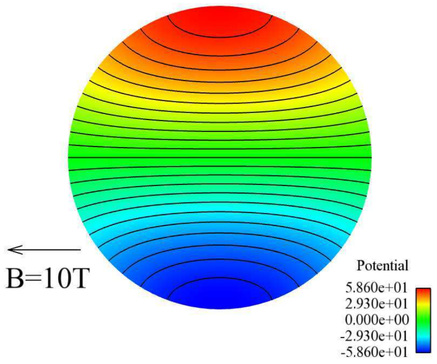

Figure 7: Gold validation. Potential along a transverse cutplane. Left: $\boldsymbol{B} = 10\,T$, scale $[-58.6, 58.6]mV$. Right: $\boldsymbol{B} = 100\,T$, scale $[-274, 274]mV$.

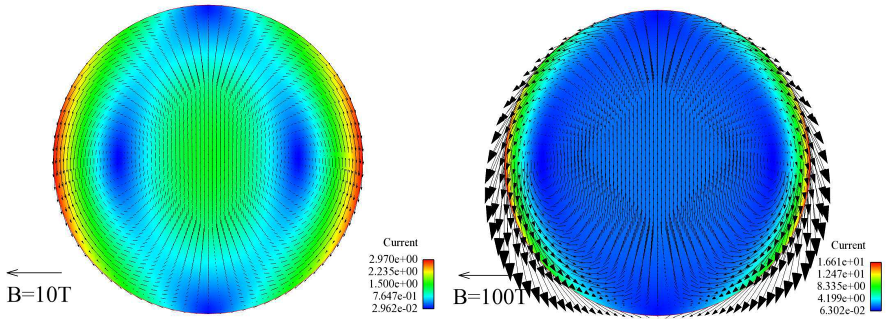

Figure 8: Gold validation. Electrical current modulus along a transverse cutplane. The arrows represent the current vector field. Left: $\boldsymbol{B} = 10\,T$, scale $[0, 2.97]A\ m^{-2}$. Right: $\boldsymbol{B} = 100\,T$, scale $[0, 16.61]A\ m^{-2}$.

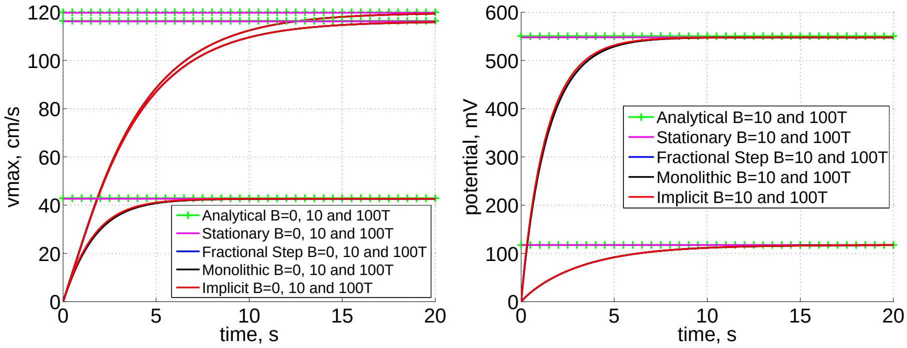

Figure 9: Gold validation. Maximum velocity (left, $cm\ s^{-1}$) and potential (right, mV) as a function of time (s) for various values of $\boldsymbol{B}$. The stationary analytical and numerical solutions are reported. The transient solutions converge toward the stationary state. For a given $\boldsymbol{B}$, the curves corresponding to the different numerical methods (fractional step: (14), monolithic: (15) with $\theta = 0$, implicit: (15) with $\theta = 1$) are almost superimposed. Left: the three sets of curves correspond to $\boldsymbol{B} = 0\,T$ (top curves), $\boldsymbol{B} = 10\,T$ and $\boldsymbol{B} = 100\,T$ (bottom curves). Right: $\boldsymbol{B} = 10\,T$ (bottom) and $\boldsymbol{B} = 100\,T$ (top). Time step $\tau = 0.01s$.

4.1.3 Comparison with a numerical solution from literature

In [18], a two-dimensional model was proposed to study the electric potential induced by the MHD effects in the aorta. We now compare these results with those given by the solution of the three-dimensional MHD model (16) coupled to the diffusion in the torso (11).

The parameters and the geometrical configurations of these experiments are reported in Table 5 and Figure 10. In the “one-aorta” case, a pressure drop $G = 24g\ cm^{-2}\ s^{-2}$ is imposed between the inlet and the outlet of a straight tube representing the aorta. The aorta is surrounded by a thin wall with a conductivity different from that of the tissue. The torso is assumed to be a cylinder of radius $7cm$ centered on the aorta. In the “two-aorta” case, the data are similar, except that two tubes are present in the torso. They are separated by $6cm$, and have opposite pressure gradients. The torso is modeled as a cylinder of radius $12cm$ centered on the descending aorta. The magnetic field $\boldsymbol{B}$ is imposed along the Ox axis (back–front axis), i.e. orthogonal to the ascending aorta. Note that it is not along the main body axis (feet–head axis) as it should be for the MRI simulations. This is an obvious limitation due the bi-dimensional nature of the computations presented in [18]. Since our purpose is here to compare our results, we keep the Ox orientation in our tri-dimensional test case. Of course, the orientation will be along Oz when the realistic configuration will be considered.

When $\boldsymbol{B} = 0T$, a standard Poiseuille flow is obtained, with an analytic mean flow $Q_a = \frac{\pi a^4}{8\eta} G \approx 188.49cm^3\ s^{-1}$, for a mean velocity $\bar{v}_a = 60cm\ s^{-1}$. On a mesh with 330 000 tetrahedra, the numerical values are $Q_{3D} = 194.09cm^3\ s^{-1}$ and $\bar{v}_{3D} = 61.8cm\ s^{-1}$, which corresponds to an error of 3%. The same mesh was used to compare our solutions with the ones of [18]. We obtained very similar results, as shown in Figure 11 and Table 6. In Figure 12, we also report the flow reduction as a function of the imposed magnetic field. Again, our results are in very good agreement.

	Parameters	Value	units
a	inner radius	1.	cm
h	wall thickness	0.22	cm
ρ	blood density	1.	$g\ cm^{-3}$
η	blood viscosity	0.05	Poise
G	pressure drop	24	$g\ cm^{-2}\ s^{-2}$
$\bar{v}$	mean velocity	60	$cm\ s^{-1}$
σ_b	blood conductivity	5.10^{-3}	$S\ cm^{-1}$
σ_w	wall conductivity	$1.5\,10^{-3}$	$S\ cm^{-1}$
σ_t	tissue conductivity	$2\,10^{-3}$	$S\ cm^{-1}$

Table 5: Data for a comparison with [18].

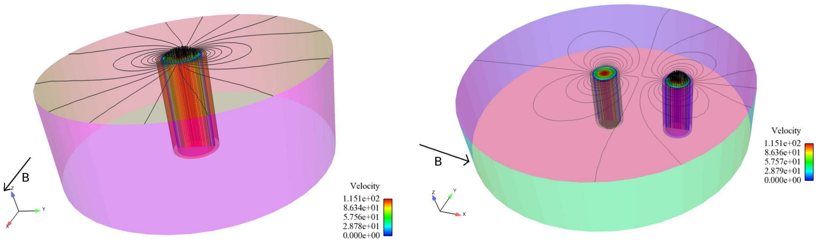

Figure 10: View of the 3D computational domains in the one-aorta (left) and two-aorta (right) configurations from [18]. We also plot the velocity along the artery and a contour of potential lines on the top. $\boldsymbol{B} = 10T$ along the Ox axis.

In Figure 13, the voltage across the aorta and the inlet flux is shown as a function of time. The transient simulations tend to the stationary values. Once again, with the considered time step, there are almost no differences between the three schemes (14), (15) with $\theta = 0$ and 1.

Potential	$A(mV)$	$B(mV)$	$\max(mV)$
our 3D computation	0.83	1.17	4.48
literature	0.83	1.18	4.44

Table 6: Comparison between [18] and our 3D computation for $\boldsymbol{B} = 1T$. Case of one-aorta: we look at two points A and B considered in [18] and the maximum value (computed on the aorta wall).

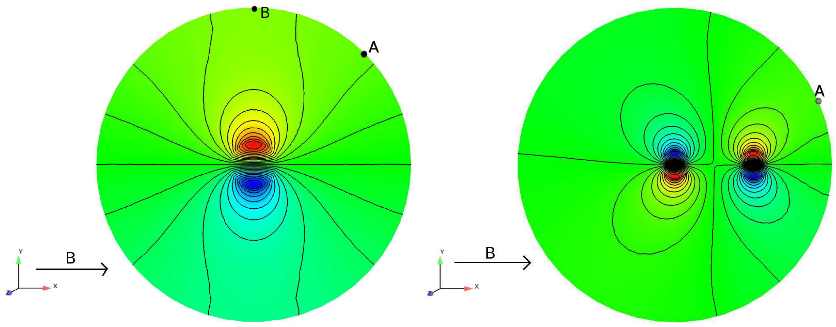

Figure 11: Potential obtained from 3D computations in the one-aorta (left) and two-aorta (right) configurations from [18]. We only plot the top of the domain. $\boldsymbol{B} = 1T$ along the Ox axis. The equipotential lines are very similar to the ones of [18]. The location of the point A (and B in the left figure) is indicated by a dot. The computed potential are: $\phi^1_{A,c} \approx 0.83mV$ and $\phi^1_{B,c} \approx 1.17mV$ (left) and $\phi^2_{A,c} \approx 0.57mV$ (right). They are almost the same as the values reported in [18]: $\phi^1_{A,K} = 0.83mV$, $\phi^1_{B,K} = 1.18mV$ and $\phi^2_{A,K} = 0.57mV$.

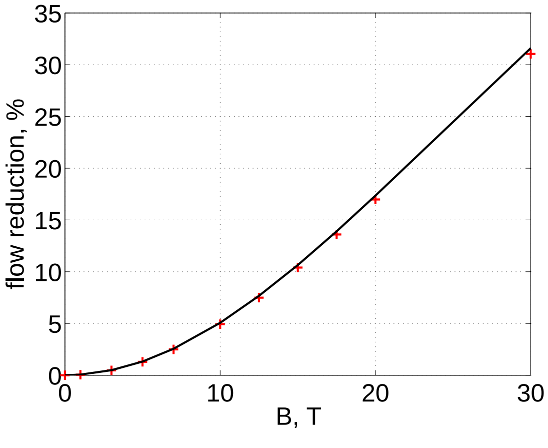

Figure 12: Percentage of flow reduction as a function of the imposed static magnetic field $\boldsymbol{B}$ (T) (one-aorta case): comparison between the values given by [18] (crosses), and the values obtained with a stationary 3D computation (solid line).

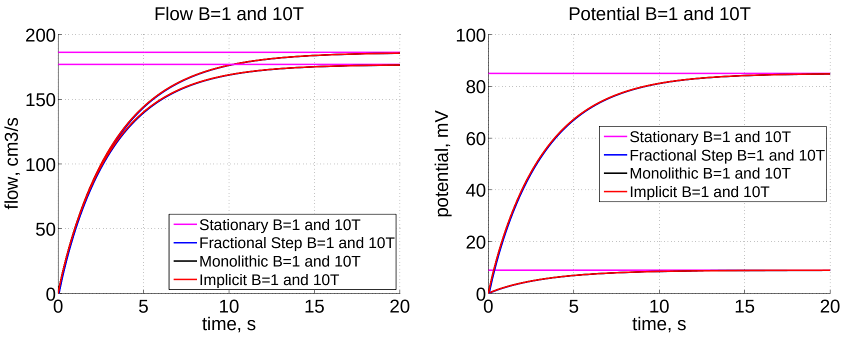

Figure 13: Kinouchi validation (one-aorta case). Flow (left, $cm^3\ s^{-1}$) and potential (right, mV) as a function of time (s) for $\boldsymbol{B} = 1T$ and $\boldsymbol{B} = 10T$. The transient solutions converge toward the numerical stationary state. For a given $\boldsymbol{B}$, the curves corresponding to different numerical methods (fractional step, monolithic, implicit) are almost superimposed. Left: the two sets of curves correspond to $\boldsymbol{B} = 1\,T$ (top curves) and $\boldsymbol{B} = 10\,T$ (bottom curves). Right: $\boldsymbol{B} = 10\,T$ (top) and $\boldsymbol{B} = 1\,T$ (bottom). Time step $\tau = 0.05s$.

4.1.4 Conclusion of the verification tests

All the verification tests presented above gave satisfactory results. Comparisons of the numerical solutions of the inductionless MHD (5) equations with the analytical solutions of the original MHD system (3) have confirmed the validity of the approximation for blood flows with magnetic fields up to $100T$. The coupling strategy of Section 3.3 is also validated. Moreover, the transient simulations done with (14) — which is the cheapest time scheme among the three considered — proved to be accurate and stable. This scheme will therefore be used for the more realistic configuration addressed in the next section.

4.2 MHD effects on the ECG

This section contains the main results of this study. The three models — MHD in the aorta (5), bidomain in the heart (7) and diffusion in the torso (11) — are coupled together and solved on a realistic anatomy.

4.2.1 Mesh, time step and data considerations

The body mesh contains three regions with different conductivities: bones in the torso, lungs and remaining parts. A heart, limited to two ventricles, and a large portion of an aorta are inserted in the body. The aorta comes from [21], all the other parts come from Zygote Media Group, Inc. The three subdomains — aorta, heart, body — were meshed separately using ghs3d [11], see Table 7 and Figure 14. The three resulting meshes are conforming, *i.e.* match at their interfaces.

The electrocardiograms are obtained by plotting linear combinations of the values of ϕ_{T} on 9 standardized points of the body surfaces (Figure 15). We refer to [19] p. 277 or [3] for the definition of these quantities.

Mesh	# vertices	# tetrahedra
heart	108 112	541 994
aorta	22 798	110 362
body	264 010	1 437 391

Table 7: Meshes for the heart, the aorta and the rest of the body.

The time step was $\tau = 0.25ms$ for all computations in order to model accurately the electrophysiology. As observed in [3], larger time steps produce undesirable spurious oscillations during the QRS complex. The mesh of the heart was chosen fine enough to capture the front propagation. Several computations were made with different mesh refinements of the aorta but they showed little differences in the ECG (less than 2% change in the peak value).

The data used for the computations are given in Tables 10–13 in Annex A. There is quite a large variability in the values of conductivity data [7, 29, 19], we took values from [26]. The blood inside the ventricles is assumed to be still and is treated as a passive diffusive domain.

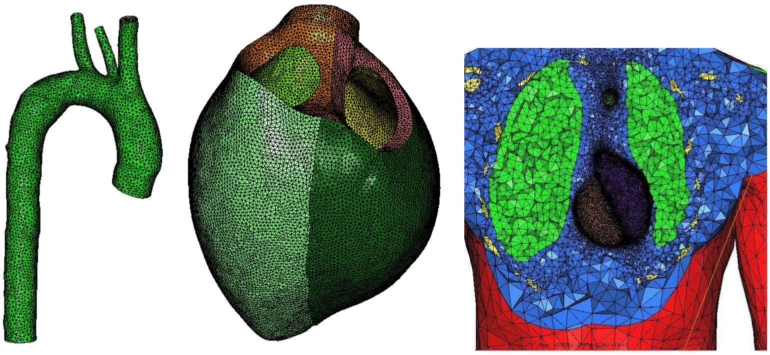

Figure 14: Meshes of the three domains: aorta, heart and body (split view of the torso; one can see the subdomains representing the lungs, bones and ventricles).

4.2.2 Electrocardiograms with MHD effects

In Figure 16, we show the flow Q imposed at the inlet of the aorta. We also report the ECG and the inflow in the same picture, in order to show how the velocity pulse is located in time with respect to the cardiac cycle: the ejection of blood in the aorta follows immediately the QRS complex (R is the first large peak in the ECG), *i.e.* the contraction of the left ventricle. The T-wave (secondary peak), occurs approximately at $t = 250ms$.

The 12-lead ECGs represented in Figure 17 have been obtained by solving the full coupled problem with $B = 0, 3, 8$ and $10\ T$. With $B = 0$, the results are similar to those presented in [3, 5]: the peak during the QRS complex is approximately $1.8mV$ for the lead I, and the peak during the T-wave reaches approximately $0.8mV$. The precordial leads V_3, V_4 and V_5 are almost unaffected

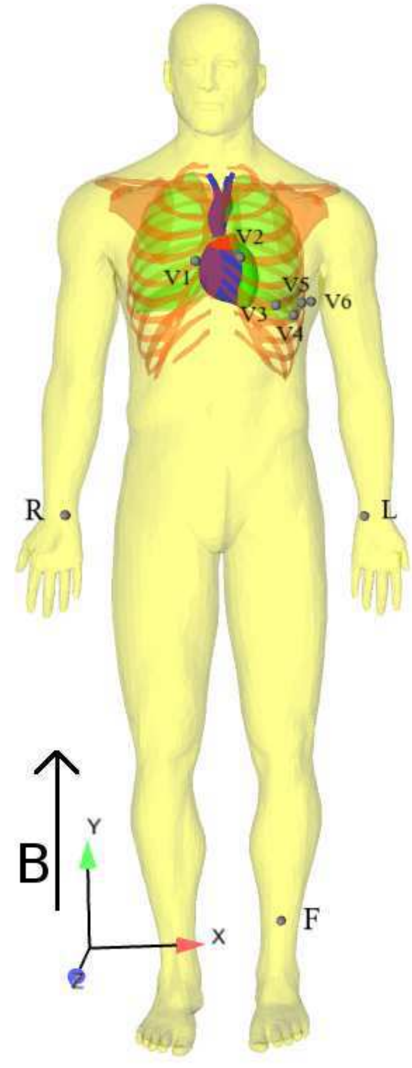

Figure 15: Body domain showing the 9 points on the skin that are used to compute the ECG. The magnetic field is imposed along the main body axis (Oy).

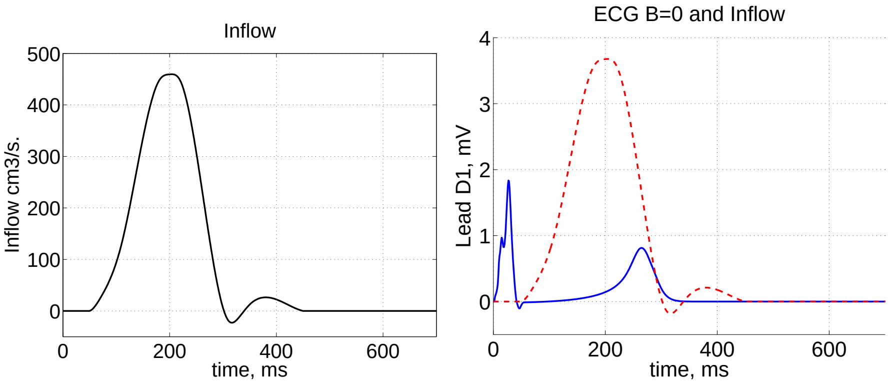

Figure 16: Left: imposed inlet flow Q $(cm^3\ s^{-1})$ as a function of time (ms). The total flux is approximately $5L\ min^{-1}$. Right: lead I of the ECG with $\boldsymbol{B} = 0$, in mV (solid line). The dashed-line represents a rescaled inflow.

by the magnetic field. In all other leads, the T-wave is altered by the MHD in the aorta, and this effect is amplified when $\boldsymbol{B}$ increases. The MHD effect is particularly strong for the limb leads I, II, III, the augmented limb leads aVR, aVL and for the precordial lead V_1. In Table 8, we report for various $\boldsymbol{B}$ the extremal values of the electric potential in the aorta and on the body surface, as well as the peak values of the leads I, II and III, and the maximum electrical current intensity in the aorta. Looking at the lead I (Figure 18), the T-wave peak increases from $0.8mV$ when $\boldsymbol{B} = 0T$, to $1.6mV$ when $\boldsymbol{B} = 3T$, and up to $3.85mV$ when $\boldsymbol{B} = 8T$. Considering the leads II and III, the effect is not as important. The maximum value increases linearly with $\boldsymbol{B}$, see Figure 19. These results are in relatively good agreement with those of [15], although the ECG given in their Fig.1 shows an MHD effect more pronounced than ours for lead II. Different experimental values are reported in the literature for the T-wave elevation during MRI examinations: Nijm *et al.* [23] measured a T-wave elevation of order $0.2mV$ for healthy subjects inside a $3T$ MRI scanner. Abi-Abdallah *et al.* [2] found increases between 0.2 and $0.7mV$ (about 300% increase) for subjects exposed to a 1.5 Tesla magnet. Chakeres *et al.* [4] provided ECG recordings during exposure to 0, 1.5, 3, 4.5, 6 and 8 Tesla and noted that the distortions of the ECGs are amplified with increasing magnetic field strength. Unfortunately, they do not give any scale for these ECGs recordings; consequently, no quantitative comparison is possible.

In the ECG perturbed by the MHD, the T-wave has a duration in time of $\approx 200ms$ (over a $700ms$ cardiac cycle), see Figure 17. This is consistent with the observations of [4] (Fig. 6) or [2] (Fig. 1).

From Figures 18 and 20, one notices that the ECG is, with a good approximation, the superposition of the ECG without magnetic field and of the MHD signal, that is proportional to the magnetic field $\boldsymbol{B}$ and to the flux Q in $(cm^3\ s^{-1})$:

$$D_i(B) \approx D_i(B = 0) + \alpha_i B\, Q \quad (mV), \tag{19}$$

where D_i is the i^{th} lead and the coefficients α_i, $i = 1, \ldots, 12$, are given in Table 9. The equation (19) is a good approximation for almost all leads, except

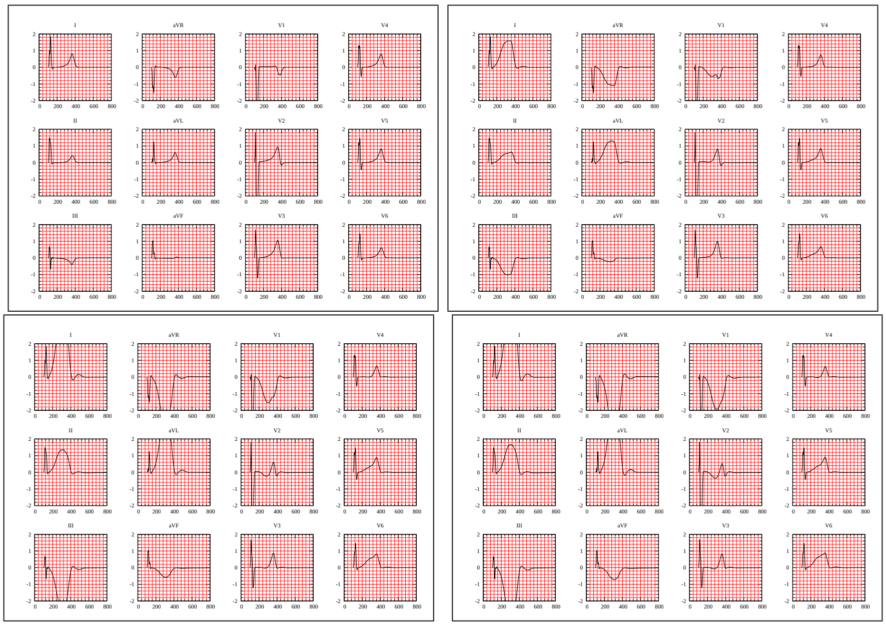

Figure 17: Standard 12-lead ECG with MHD effects as a function of B. From top to bottom, $B = 0,\ 3,\ 8,\ 10\,T$. Potential in $[-2, +2]mV$, time in $[0, 800]ms$.)

Wave	$\boldsymbol{B}$ (T)	*Ha*	$\phi_{\rm A}^{\rm min}$	$\phi_{\rm A}^{\rm max}$ (mV)	$\Delta\phi_{\rm A}$	$\phi_{\rm S}^{\rm min}$	$\phi_{\rm S}^{\rm max}$ (mV)	$\Delta\phi_{\rm S}$	Lead *I*	Lead *II* (mV)	Lead *III*	$\lVert\boldsymbol{j}_A\rVert^{\max}$ ($A\,m^{-2}$)
R	all		-4.9	1.9	6.8	-6.3	2.0	8.3	1.83	1.47	0.66	0.23
T-wave	0	0	-0.5	-0.02	0.48	-0.06	0.5	0.56	0.81	0.42	-0.40	0.039
	1	0.12	-9.7	8.5	18.2	-1.0	1.23	2.23	1.05	0.49	-0.57	0.61
	2	0.24	-19.5	17	36.5	-2.0	2.35	4.35	1.30	0.56	-0.76	1.22
	3	0.36	-29	25.6	54.6	-3.0	3.33	6.33	1.59	0.64	-1.02	1.84
	5	0.59	-49	43	92	-4.9	5.7	10.6	2.49	0.87	-1.61	3.06
	8	0.95	-78	68	146	-8.1	8.85	16.9	3.85	1.35	-2.50	4.90
	10	1.19	-97	86	183	-9.8	11	20.8	4.76	1.67	-3.10	6.13
	15	1.78	-146	128	274	-15	16.6	31.6	7.05	2.47	-4.58	9.19
	20	2.38	-195	171	366	-20	22	42	9.34	3.27	-6.08	12.2

Table 8: Potential and current as a function of $\boldsymbol{B}$: maximum and minimum potentials in the aorta ($\phi_{\rm A}$) and on the skin ($\phi_{\rm S}$), peak value for leads *I*, *II* and *III*, peak current modulus in the aorta ($\boldsymbol{j}_A$). Values at $t \approx 210ms$, peak value for the MHD effects (T-wave), and value during the R-wave at $t = 27ms$ (it is identical for all $\boldsymbol{B}$). The Hartmann number is computed as $Ha = \boldsymbol{B}\, R_A \sqrt{\boldsymbol{\sigma}_{\rm bl}/\eta}$, see Table 11.

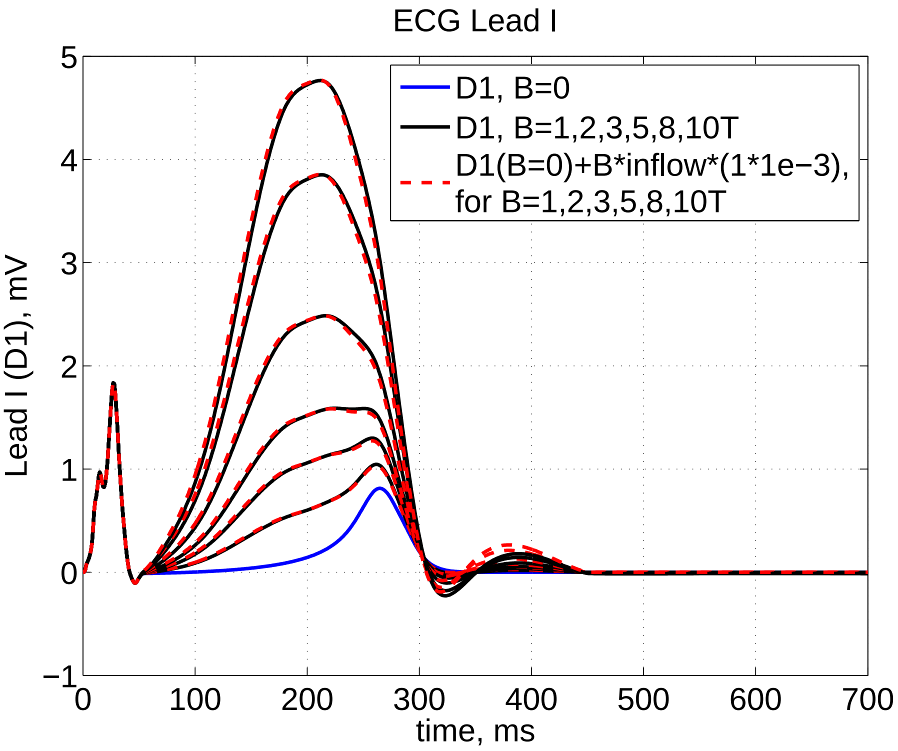

Figure 18: Lead I (D_1) with MHD for various $B = 0,\,1,\,2,\,5,\,8\,10\,T$. The ECG are drawn with solid lines, and the secondary peak increases with B. The dashed lines represent the functions $D_1(B = 0) + \alpha_1 B\,Q$.

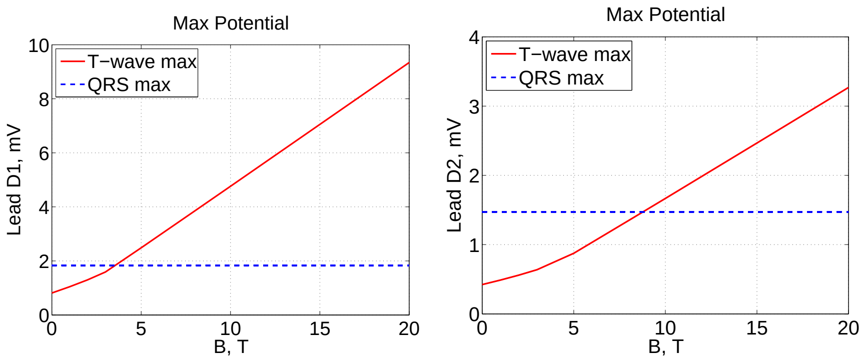

Figure 19: Maximum potential value for leads I and II (mV) as a function of $\boldsymbol{B}$. The R value is recalled (horizontal line).

some precordial leads, particularly V_3 and V_4. Note that it was *not* obvious *a priori* that such a simple formula would hold.

It might be feared that the MHD effect in the aorta induces a perturbation of the electrical activity of the heart, and possibly lead to fibrillation. According to our computations, this does not happen, even for strong magnetic field: the extracellular potential in the myocardium is only slightly modified by the aortic electrical activity, see Figure 21.

	$I(D_1)$	$aVR(D_4)$	$V_1(D_7)$	$V_4(D_{10})$
α_i	$1.\ 10^{-3}$	$-0.67\ 10^{-3}$	$-0.43\ 10^{-3}$	$-0.05\ 10^{-3}$
	$II(D_2)$	$aVL(D_5)$	$V_2(D_8)$	$V_5(D_{11})$
α_i	$0.35\ 10^{-3}$	$0.82\ 10^{-3}$	$-0.14\ 10^{-3}$	$0.05\ 10^{-3}$
	$III(D_3)$	$aVF(D_6)$	$V_3(D_9)$	$V_6(D_{12})$
α_i	$-0.65\ 10^{-3}$	$-0.15\ 10^{-3}$	$-0.075\ 10^{-3}$	$0.12\ 10^{-3}$

Table 9: Proportionality coefficients in the numerical relation (19). α_i in $10\ cm^{-1} = mm^{-1}$.

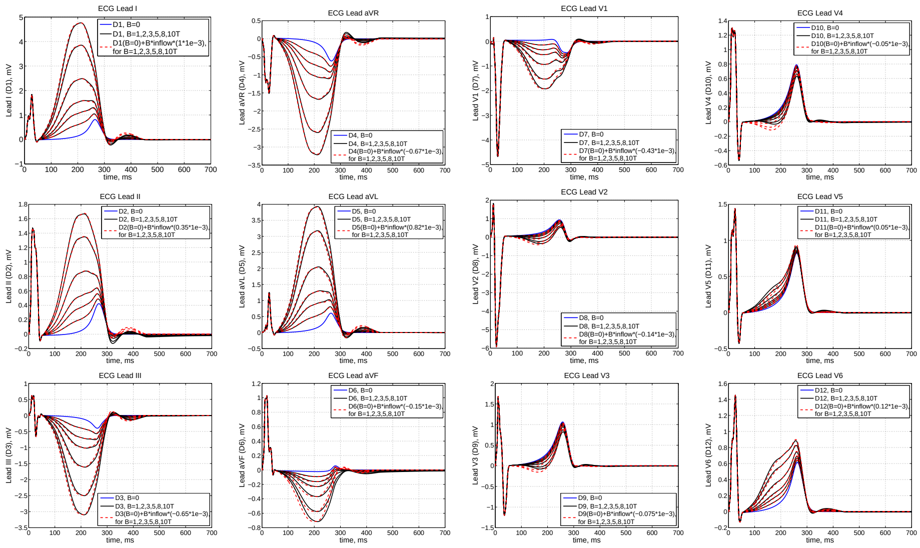

Figure 20: 12-leads $D_i(B)$ with MHD for various $B = 0, 1, 2, 3, 5, 8, 10\,T$. The scales vary in each case. The ECG are drawn with solid lines, and the secondary peak increases with $\boldsymbol{B}$. The dashed lines represent the functions $D_i(B = 0) + \alpha_i BQ(cm^3\ s^{-1})$.

We also performed a computation using the weak coupling strategy, see Figure 22 and Remark 2.1. This simplification results in a modification of the amplitude in the QRS complex and in the T-wave, but with no clear pattern, as it can either increase or decrease their relative amplitudes, see the leads I

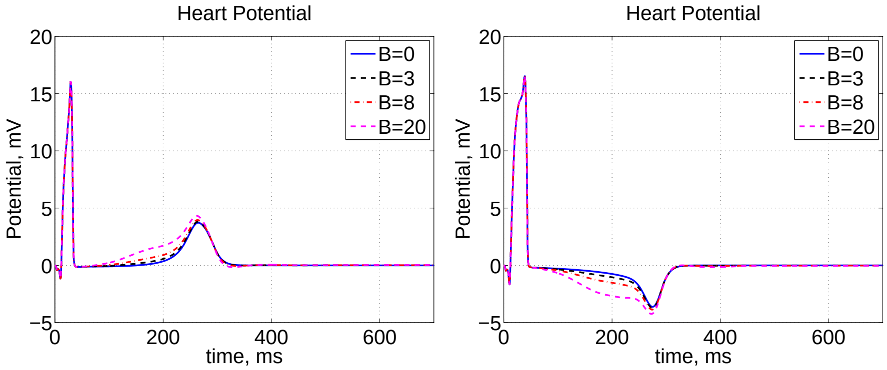

Figure 21: Potential (mV) at two different locations (left and right figures) on the heart surface as a function of time (ms), for $\boldsymbol{B} = 0, 3, 8, 20T$. The two different points on the heart are chosen so as to show the strongest MHD effect.

and II in Figure 22 for $B = 10T$. The weak coupling simplification is therefore questionable to assess the MHD effects on the ECG.

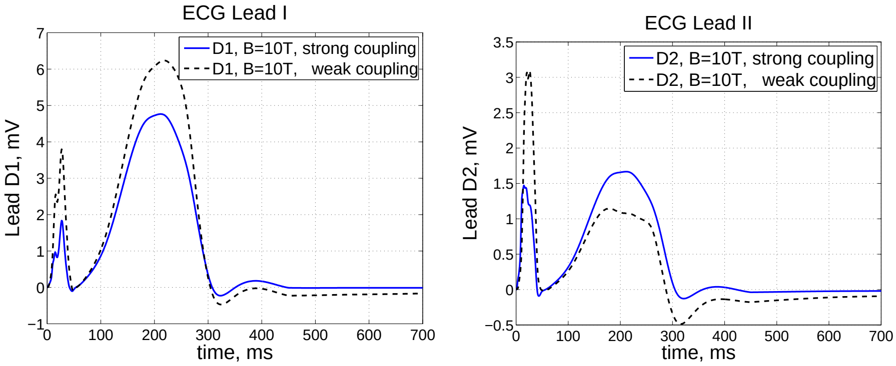

Figure 22: Leads I (Left) and II (Right) with MHD effects $(\boldsymbol{B} = 10T)$. Comparison between the strong coupling strategy (solid line) and the weak coupling strategy (dashed line).

4.2.3 MHD effect on the aorta and on the body

The $3D$ numerical computations can provide many details: in Figure 23, the electric potential on the skin is represented at various time instants for $B =$ 0, 1, 3, $8T$. One can see the effects of the electrical activity of the heart particularly during the QRS complex and the T-wave. The MHD effect in the aorta clearly modifies the potential around $t = 200ms$.

The velocity inside the aorta is almost unaffected by the MHD effect, even for large magnetic fields (Figure 24). This observation is consistent with the calculations given in [1] and with the results of Sections 4.1.2 and 4.1.3. The electric potential on the boundary of the aorta is represented in Figure 25. The heart activity modifies the potential of the aorta during the QRS complex ($t \approx$

$20 ms$) and has little impact during the diastole ($t \approx 200ms$). The maximum voltage due to MHD appears, as expected, across the aortic arch, where the velocity is roughly orthogonal to the applied magnetic field. The predicted values are of order $10\,mV$ to $100\,mV$, which is in agreement with the calculations of [1] and of [18].

The electrical current is represented in Figure 26 and its maximum value is reported in Table 8 for various $\boldsymbol{B}$. The current intensity is the largest on the top and on the bottom of the aortic arch, near the aortic wall. This is in agreement with the Gold simulations (Figure 8). The electrical current density of these simulations seems quite high: at $\boldsymbol{B} = 1T$, the maximum electrical current in the aorta $\boldsymbol{j}_A$ is approximately $0.6A\,m^{-2}$. It reaches approximately $1.8A\,m^{-2}$ at $3T$ and $4.9A\,m^{-2}$ at $8T$. These values are consistent with the simple evaluation of $|\boldsymbol{j}_A| \approx \boldsymbol{\sigma}_{\text{bl}} \frac{\Delta\phi_A}{2R_A}$, where the radius of the aorta R_A at the arch is given in Table 11. Note that the value of the current at $Ha = 1$ is $\approx 5.1A\,m^{-2}$ (interpolated from the values at $\boldsymbol{B} = 8T$ and $\boldsymbol{B} = 10T$), *i.e.* roughly twice the value obtained in the Gold test case, $2.9A\,m^{-2}$ see Table 4.

This difference can be explained by a larger maximum velocity, a more complex geometry (non infinite tube, outlets, ...), and a coupling with the surrounding tissue (non insulating walls).

These current intensity values should also be compared to the current densities generated by the cardiac activity that reach approximately $1A\,m^{-2}$ inside the heart [30]. However, it should be noted that the current is large only in a small region of the aortic arch, and the diffusion process from the aortic arch to the heart in the torso decreases significantly the potential due to the MHD. In [18, 30], the authors predicted a maximum current of $1.15A\,m^{-2}$ at $5T$, $2.20A\,m^{-2}$ at $10T$ and $3.20A\,m^{-2}$ at $15T$. This is from two to three times smaller than our values. Two factors can explain these differences. Firstly, as recalled in Section 4.1.3, the orientation of $\boldsymbol{B}$ is not along the main body axis in [18]. Secondly, the flow pattern obtained in our realistic aortic arch solving the nonlinear Navier-Stokes equations is of course very far from a steady state flow in an infinite cylinder. The induced electrical current has therefore a much more complicated behavior than in the simplified models.

5 Conclusions

A model made of three components has been proposed: electrophysiology in the heart, MHD in the aorta and electrostatics in the rest of the body. A standard 12-lead ECG has been computed with and without magnetic field. A larger T-wave was obtained in presence of a magnetic field, as expected. The electric potential and the electrical current in the aorta has been computed. The impact of the MHD effect on the electric activity of the heart has been evaluated and seems limited, even for strong magnetic fields.

The model, although quite complex, could still be improved. For example, the blood flow might be also considered in the pulmonary artery and in the heart; the elasticity of the aorta could be considered as in [21]. Another improvement could be to link directly the aortic to an electromechanical model of the myocardium [5].

The data for the conductivities of different tissues used in the literature [25, 18] can vary by an order of magnitude. It should thus be interesting to perform

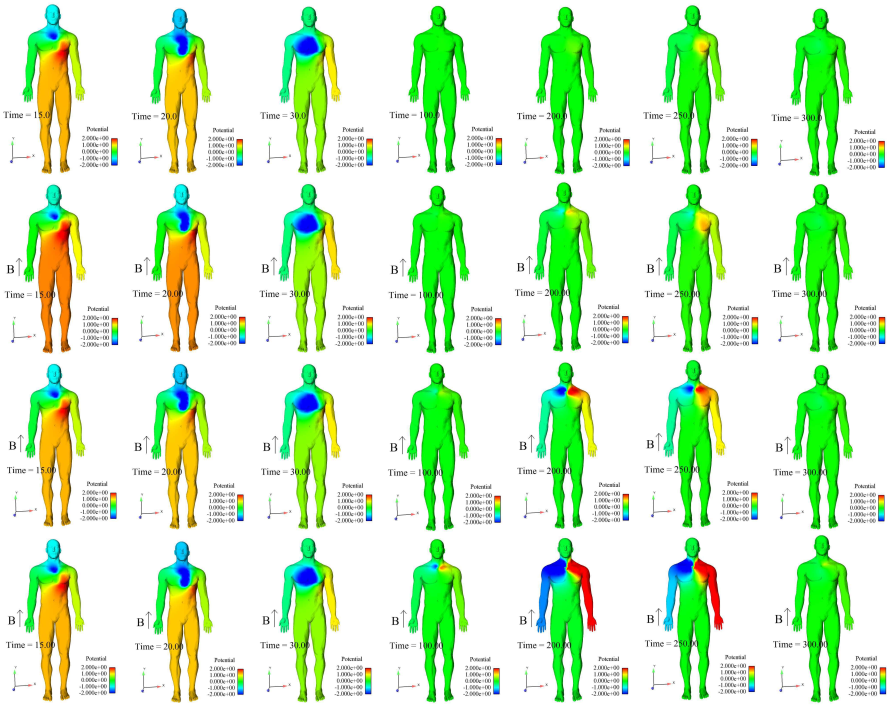

Figure 23: View of the electric potential on the skin at different times as a function of B. From top to bottom: $B = 0T$ (no MHD), $B = 1,\ 3,\ 8T$. From left to right, time instants: $t = 15ms, 20ms, 30ms, 100ms, 200ms, 250ms, 300ms$. Scale: $[-2, 2]mV$.

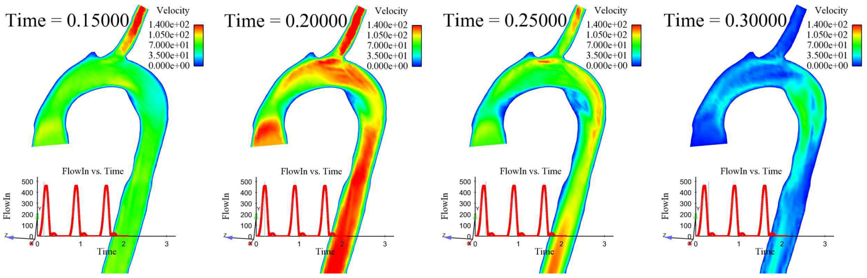

Figure 24: Norm of the velocity in the aorta, along a cut plane. The velocity is almost identical for all B in $[0, 10T]$. From left to right, time instants: $t = 150ms, 200ms, 250ms, 300ms$. Scale: $[0, 140]cm\ s^{-1}$. Bottom curve: flow as a function of time.

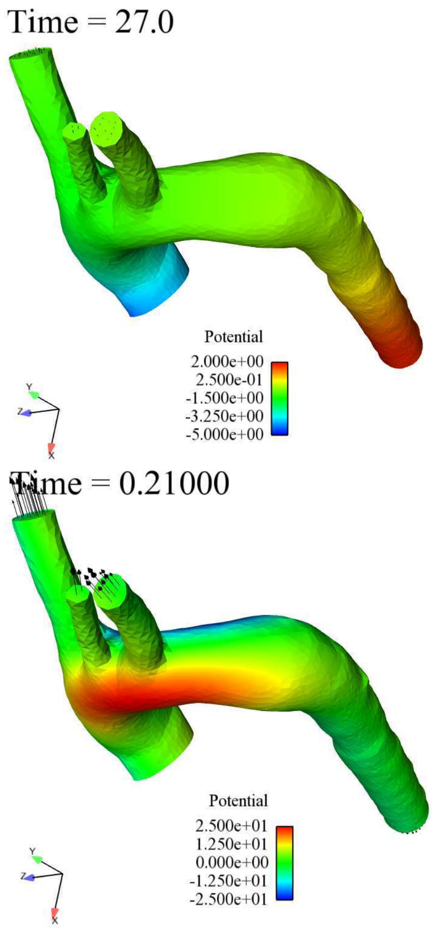

Figure 25: View of the electric potential on the aorta. Top left: potential during the QRS complex ($t = 27ms$) for all $\boldsymbol{B}$ (scale: $[-5, 2]mV$). Other images: potential during systole ($t = 210ms$) for $\boldsymbol{B} = 0T$ (top right, scale: $[-0.5, 0]mV$), for $\boldsymbol{B} = 3T$ (bottom left, scale: $[-25, 25]mV$) and for $\boldsymbol{B} = 8T$ (bottom right, scale: $[-70, 70]mV$).

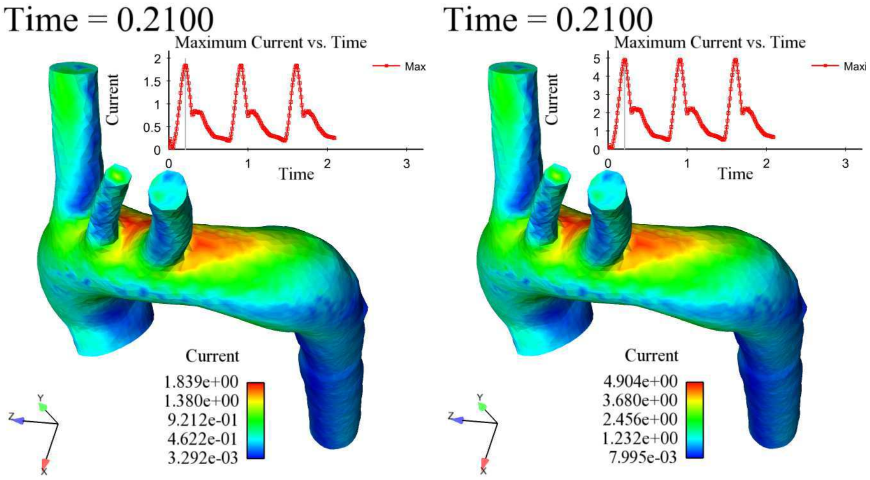

Figure 26: View of the electrical current intensity on the aorta at $t = 210ms$ (systole). Left: $\boldsymbol{B} = 3T$ (scale: $[0, 1.84] A\ m^{-2}$). Right: $\boldsymbol{B} = 8T$ (scale: $[0, 4.9] A\ m^{-2}$).

some sensitivity analysis in order to evaluate the impact of these conductivity values on the MHD effect.

The objective of the present study was to demonstrate that the computational tool was able to capture a phenomenon that has actually been observed in MRI machines. In the future, the model could be used for more interesting purposes: for example optimize the electrode locations to be less sensitive to the MHD effect, or on the contrary to extract from the MHD effect more information about the flow or the electrical properties of the tissues.

Acknowledgment: The authors wish to thank Charles Taylor and Alberto Figueroa for the mesh of the aorta.

A Data values

In this paper, the MHD computations are performed using the $\{cm,\ g,\ s,\ mA\}$ system, that has the advantage of giving a proper scaling for the blood flow, while preserving the magnetic field unit. For convenience, in the results, the electric potential is given in mV and the current in $A\ m^{-2}$. The conversion between the International System and the $\{cm,\ g,\ s,\ mA\}$ system is provided in Annex B for the main variables.

The computations of Section 4.2 use the following data. See Table 10 for the heart, Tables 11 and 12 for the aorta, and Table 13 for the body. In all these Tables, “cond” stands for “electric conductivity”.

The scaling of the MHD equation (5) and the one of the bidomain and body equations (7),(11) are different. The coupling between these two systems involves only the electric potential ϕ and the integral of the current density over

	Parameters	Value	units
$T^\star$	time period	700	ms
L	mesh dimension	≈ 10	cm
$\sigma_{i,l}$	intern longitudinal cond	$3.0\ 10^{-3}$	$S\ cm^{-1}$
$\sigma_{i,t}$	intern transverse cond	$3.0\ 10^{-4}$	$S\ cm^{-1}$
$\sigma_{e,l}$	extern longitudinal cond	$3.0\ 10^{-3}$	$S\ cm^{-1}$
$\sigma_{e,t}$	extern transverse cond	$1.2\ 10^{-3}$	$S\ cm^{-1}$
ϕ_{H}	electric potential	≈ 10	mV

Table 10: Main parameter values in the heart. See [3] for more details.

	Parameters	Value	units
$T^\star$	time period	0.7	s
L	mesh dimension	≈ 10	cm
R_A	aortic arch radius	≈ 0.95	cm
ρ	blood density	1.06	$g\ cm^{-3}$
η	blood viscosity	0.04	$g\ cm^{-1}\ s^{-1}$
$\boldsymbol{\sigma}_{\mathrm{bl}}$	blood conductivity	$6.25\ 10^{-4}$	$\frac{mA^2\ s^3}{g\ cm^3}$
$\boldsymbol{B}$	magnetic field	1 to 20	T
$\overline{u}_{\max}$	mean inlet velocity	98	$cm\ s^{-1}$
$q_{\max}$	max blood flow	460	$cm^3\ s^{-1}$
S	inlet area	4.66	cm^2
Q	blood flow rate	≈ 5.36	$L\ min^{-1}$
ϕ_{A}	electric potential	≈ 100	$\frac{g\ cm^2}{s^3\ mA}$

Table 11: Main parameter values in the aorta expressed in $\{cm,\ g,\ s,\ mA\}$. $\overline{u}_{\max}$ denotes the maximum mean blood velocity at the inlet (during systole).

	R_p	R_d	C
Outlet$_1$	$0.050\,10^4$	$0.85\,10^4$	$0.95\,10^{-4}$
Outlet$_2$	$0.191\,10^4$	$3.22\,10^4$	$0.25\,10^{-4}$
Outlet$_3$	$0.075\,10^4$	$1.26\,10^4$	$0.64\,10^{-4}$
Outlet	$0.015\,10^4$	$0.25\,10^4$	$3.17\,10^{-4}$

Table 12: Values of the windkessel models for the aorta: proximal R_p and distal R_d resistivities and capacitance C for all outlets. Units in cm, g, s (R in $dynes\ s\ cm^{-5}$ and C in $cm^5\ dynes^{-1}$).

	Parameters	Value	units
L	mesh dimension	≈ 100	cm
$\boldsymbol{\sigma}_{\mathrm{T}}$	tissue cond	$6.\ 10^{-4}$	$S\ cm^{-1}$
$\boldsymbol{\sigma}_{\mathrm{bl}}$	blood cond	$6.25\ 10^{-3}$	$S\ cm^{-1}$
$\boldsymbol{\sigma}_{bone}$	bone cond	$5.65\ 10^{-5}$	$S\ cm^{-1}$
$\boldsymbol{\sigma}_{l}$	lung cond	5.10^{-4}	$S\ cm^{-1}$
ϕ_{T}	electric potential	≈ 10	mV

Table 13: Main parameter values in the body.

a surface Σ defined by

$$J \overset{\mathrm{def}}{=} \int_{\Sigma} \boldsymbol{j} \cdot \boldsymbol{n} \, d\Sigma (= \int_{\Sigma} \sigma \boldsymbol{\nabla} \phi \cdot \boldsymbol{n} \, d\Sigma).$$

The coupling is performed using the conversions of Table 14. The units used by the master (see Section 3.3) in the transfers are: ϕ in mV and J in mA.

input			output	
ϕ_{A}	$1 \dfrac{g\ cm^2}{s^3\ mA}$	$\longrightarrow$	$\phi_{\mathrm{H}},\, \phi_{\mathrm{T}}$	$0.1\, mV$
$\phi_{\mathrm{H}},\, \phi_{\mathrm{T}}$	$1\, mV$	$\longrightarrow$	ϕ_{A}	$10 \dfrac{g\ cm^2}{s^3\ mA}$
J_A	$1\, mA$	$\longrightarrow$	$J_H,\, J_T$	$1\, S\, mV$
$J_H,\, J_T$	$1\, S\, mV$	$\longrightarrow$	J_A	$1\, mA$

Table 14: Scaling for the coupling between the three subdomains. Note that $1\, S\, mV = 1\, mA$.

B Conversion from SI units into {cm/g/s/mA}

The conversion between SI units and $\{cm/g/s/mA\}$ units for the main variables is given in Table 15. Note that the magnetic field unit remains unchanged in the two systems: $1T \longleftrightarrow 1\{cm/g/s/mA\}$.

	SI	$\{cm/g/s/mA\}$
p	$1Pa = 1 \dfrac{N}{m^2} = 1 \dfrac{kg}{m\ s^2}$	$10 \dfrac{g}{cm\ s^2}$
$\boldsymbol{u}$	$1 \dfrac{m}{s}$	$100 \dfrac{cm}{s}$
ρ	$10^3 \dfrac{kg}{m^3}$	$1 \dfrac{g}{cm^3}$
η	$1 \dfrac{kg}{m\ s}$	$10 \dfrac{g}{cm\ s}$
η_{bl}	$\approx 4.\ 10^{-3} \dfrac{kg}{m\ s}$	$0.04 \dfrac{g}{cm\ s}$
σ	$1 \dfrac{S}{m} = 1 \dfrac{s^3\ A^2}{kg\ m^3}$	$10^{-3} \dfrac{s^3\ mA^2}{g\ cm^3}$
$\boldsymbol{\sigma}_{\mathrm{bl}}$	$\approx 0.6 \dfrac{S}{m} = 6.10^{-3} \dfrac{S}{cm}$	$6.10^{-4} \dfrac{s^3\ mA^2}{g\ cm^3}$
$\boldsymbol{B}$	$1T = 1 \dfrac{kg}{s^2\ A}$	$1 \dfrac{g}{s^2\ mA}$
ϕ	$1V = 1 \dfrac{kg\ m^2}{s^3\ A}$	$10^4\ \dfrac{g\ cm^2}{s^3\ mA}$
ϕ	$1mV$	$10\ \dfrac{g\ cm^2}{s^3\ mA}$
$\boldsymbol{j}$	$1 \dfrac{A}{m^2}$	$10^{-1}\ \dfrac{mA}{cm^2}$

Table 15: Conversion between SI units and $\{cm/g/s/mA\}$ units.

References

[1] D. Abi-Abdallah, A. Drochon, V. Robin, and O. Fokapu. Effects of static magnetic field exposure on blood flow. *Eur. Phys. J. Appl. Phys.*, 45(1):11301, 2009.

[2] D. Abi-Abdallah, V. Robin, A. Drochon, and O. Fokapu. Alterations in human ECG due to the magnetohydrodynamic effect: a method for accurate R peak detection in the presence of high MHD artifacts. In *Conf Proc IEEE Eng Med Biol Soc.*, pages 1842–5, 2007.

[3] M. Boulakia, S. Cazeau, M.A. Fernández, J-F. Gerbeau, and N. Zemzemi. Mathematical modeling of electrocardiograms: A numerical study. *Annals of Biomedical Engineering*, 38:1071–1097, 2010.

[4] DW. Chakeres, A. Kangarlu, H. Boudoulas, and DC. Young. Effect of static magnetic field exposure of up to 8 Tesla on sequential human vital sign measurements. *J Magn Reson Imaging*, 18(3):346–352, 2003.

[5] D. Chapelle, M. A. Fernández, J-F. Gerbeau, P. Moireau, J. Sainte-Marie, and N. Zemzemi. Numerical simulation of the electromechanical activity of the heart. In *Functional Imaging and Modeling of the Heart*, number 5528 in Lecture Notes in Computer Science, pages 357–365. Springer-Verlag, 2009.

[6] J. M. Chia, S. E. Fischer, S. A. Wickline, and C. H. Lorenz. Performance of QRS detection for cardiac magnetic resonance imaging with a novel vectorcardiographic triggering method. *Journal of Magnetic Resonance Imaging*, 12(5):678–688, 2000.

[7] J. Clements, J. Nenonen, P.K.J. Li, and B.M. Horàček. Activation dynamics in anisotropic cardiac tissue via decoupling. *Annals of Biomedical Engineering*, 32(7):984–990, 2004.

[8] L. Formaggia, A. Quarteroni, and A. Veneziani, editors. *Cardiovascular Mathematics. Modeling and simulation of the circulatory system*, volume 1 of *Modeling, Simulation and Applications*. Springer, 2009.

[9] T. Frauenrath, F. Hezel, U. Heinrichs, S. Kozerke, JF. Utting, M. Kob, C. Butenweg, P. Boesiger, and T. Niendorf. Feasibility of cardiac gating free of interference with electro-magnetic fields at 1.5 Tesla, 3.0 Tesla and 7.0 Tesla using an MR-stethoscope. *Invest Radiol.*, 44(9):539–547, 2009.

[10] C.T. Gaffey and T.S. Tenforde. Alterations in the rat electrocardiogram induced by stationary magnetic fields. *Bioelectromagnetics*, 2:357–370, 1981.

[11] P.L. George, F. Hecht, and E. Saltel. Fully automatic mesh generator for 3d domains of any shape. *Impact of Comp. in Sci. ans Eng.*, 2:187–218, 1990.

[12] J-F. Gerbeau, C. Le Bris, and T. Lelièvre. *Mathematical methods for the Magnetohydrodynamics of liquid metals.* Numerical Mathematics and Scientific Computation. Oxford University Press, 2006.

[13] R.R. Gold. Magnetohydrodynamic pipe flow. part 1. *J. Fluid Mech.*, 13:505–512, 1962.

[14] J-L. Guermond, P. Minev, and J. Shen. An overview of projection methods for incompressible flows. *Comp. Meth. Appl. Mech. Engng.*, 195(44–47):6011–6045, 2006.

[15] A. Gupta, A.R. Weeks, and S.M. Richie. Simulation of elevated T-waves of an ECG inside a static magnetic field (MRI). *Biomedical Engineering, IEEE Transactions on*, 55(7):1890–1896, 2008.

[16] G. Huiskamp and A van Oosterom. The depolarization sequence of the human heart surface computed from measured body surface potentials. *IEEE Trans. Biomed. Eng.*, 35(12):1047–1058, 1988.

[17] W. Kainz, J. Guag, S. Benkler, D. Szczerba, E. Neufeld, V. Krauthamer, J. Myklebust, H. Bassen, I. Chang, N. Chavannes, J.H. Kim, M. Sarntinoranont, and N. Kuster. Development and validation of a magnetohydrodynamic solver for blood flow analysis. *Phys. Med. Biol.*, 55(23):7253, 2010.

[18] Y. Kinouchi, H. Yamaguchi, and T.S. Tenforde. Theoretical analysis of magnetic field interactions with aortic blood flow. *Bioelectromagnetics*, 17:21–32, 1996.

[19] J. Malmivuo and R. Plonsey. *Principles and Applications of Bioelectric and Biomagnetic Fields.* Oxford University Press, 1995.

[20] C.C. Mitchell and D.G. Schaeffer. A two-current model for the dynamics of cardiac membrane. *Bulletin Math. Bio.*, 65:767–793, 2003.

[21] P. Moireau, N. Xiao, M. Astorino, C. Figueroa, D. Chapelle, C. Taylor, and J-F. Gerbeau. External tissue support and fluid-structure simulation in blood flows. *Biomechanics and Modeling in Mechanobiology*, pages 1–18, 2011. 10.1007/s10237-011-0289-z.

[22] R. Moreau. *Magnetohydrodynamics.* Kluwer Academic Publishers, 1990.

[23] G.M. Nijm, S. Swiryn, A.C. Larson, and A.V. Sahakian. Characterization of the magnetohydrodynamic effect as a signal from the surface electrocardiogram during cardiac magnetic resonance imaging. In *Computers in Cardiology, 2006*, pages 269 –272, sept. 2006.

[24] G.M. Nijm, S. Swiryn, A.C. Larson, and A.V. Sahakian. Extraction of the magnetohydrodynamic blood flow potential from the surface electrocardiogram in Magnetic Resonance Imaging. *Medical and Biological Engineering and Computing*, 46(7):729–733, 2008.

[25] G.M. Nijm, S. Swiryn, A.C. Larson, and A.V. Sahakian. Inhomogeneous human torso model of magnetohydrodynamic blood flow potentials generated in the mr environment. In *Computers in Cardiology, 2008*, pages 9 –12, sept. 2008.

[26] M. Potse, B. Dubé, J. Richer, A. Vinet, and R. M. Gulrajani. A comparison of monodomain and bidomain reaction-diffusion models for action potential propagation in the human heart. *Biomedical Engineering, IEEE Transactions on*, 53(12):2425–2435, 2006.

[27] A. Quarteroni and A. Valli. *Domain decomposition methods for partial differential equations.* The Clarendon Press Oxford University Press, New York, 1999. Oxford Science Publications.

[28] F.B. Sachse. *Computational Cardiology: Modeling of Anatomy, Electrophysiology, and Mechanics.* Springer-Verlag, 2004.

[29] J. Sundnes, G.T. Lines, X. Cai, B.F. Nielsen, K.-A. Mardal, and A. Tveito. *Computing the electrical activity in the heart.* Springer-Verlag, 2006.

[30] T.S. Tenforde. Magnetically induced electric fields and currents in the circulatory system. *Progress in Biophysics and Molecular Biology*, 87:279–288, 2005.

[31] T.S. Tenforde, C.T. Gaffey, B.R. Moyer, and T.F. Budinger. Cardiovascular alterations in Macaca monkeys exposed to stationary magnetic fields: experimental observations and theoretical analysis. *Bioelectromagnetics*, 4:1–9, 1983.

[32] Z. Tse, Ch. Dumoulin, G. Clifford, M. Jerosch-Herold, D. Kacher, R. Kwong, W. Stevenson, and E. Schmidt. 12-lead ECG in a 1.5 Tesla MRI: Separation of real ECG and MHD voltages with adaptive filtering for gating and non-invasive cardiac output. *Journal of Cardiovascular Magnetic Resonance*, 12(Suppl 1):O95, 2010.

Contents

Centre de recherche INRIA Paris – Rocquencourt
Domaine de Voluceau - Rocquencourt - BP 105 - 78153 Le Chesnay Cedex (France)

Centre de recherche INRIA Bordeaux – Sud Ouest : Domaine Universitaire - 351, cours de la Libération - 33405 Talence Cedex
Centre de recherche INRIA Grenoble – Rhône-Alpes : 655, avenue de l'Europe - 38334 Montbonnot Saint-Ismier
Centre de recherche INRIA Lille – Nord Europe : Parc Scientifique de la Haute Borne - 40, avenue Halley - 59650 Villeneuve d'Ascq
Centre de recherche INRIA Nancy – Grand Est : LORIA, Technopôle de Nancy-Brabois - Campus scientifique
615, rue du Jardin Botanique - BP 101 - 54602 Villers-lès-Nancy Cedex
Centre de recherche INRIA Rennes – Bretagne Atlantique : IRISA, Campus universitaire de Beaulieu - 35042 Rennes Cedex
Centre de recherche INRIA Saclay – Île-de-France : Parc Orsay Université - ZAC des Vignes : 4, rue Jacques Monod - 91893 Orsay Cedex
Centre de recherche INRIA Sophia Antipolis – Méditerranée : 2004, route des Lucioles - BP 93 - 06902 Sophia Antipolis Cedex

Éditeur
INRIA - Domaine de Voluceau - Rocquencourt, BP 105 - 78153 Le Chesnay Cedex (France)
http://www.inria.fr
ISSN 0249-6399